

A structure-based model for turbulent-boundary-layer wall pressures

B.-K. AHN¹†, W. R. GRAHAM¹‡ AND S. A. RIZZI²

¹Department of Engineering, Trumpington Street, Cambridge, CB2 1PZ, UK

²NASA Langley Research Center, Hampton, VA 23681-2199, USA

(Received 23 July 2009; revised 27 November 2009; accepted 27 November 2009;
first published online 16 March 2010)

Practical prediction of structural vibrations due to a turbulent boundary layer currently depends on empirical representations of the unsteady wall pressures. Improvements in these representations would be greatly facilitated if a simple, physically based model were available to test *ad hoc* assumptions and provide rigorous interpolation of experimental data. A possible candidate is the attached-eddy model, developed from Townsend's initial ideas by Perry and co-workers in the context of turbulence velocity spectra. This approach employs the superposition of contributions from individual 'eddies', of varying size, to yield its predictions. It is shown here that the same methodology can be applied for wall pressures, once the field due to an eddy has been obtained via solution of the governing Poisson equation. Comparisons with large-eddy simulation and experimental data, spanning a two-decade Reynolds number range, show remarkably good agreement, given the simplicity of the model. It is concluded that this approach has the potential to provide useful physical insight and, subject to its extension to a time-resolved form, improvements to existing empirical formulations.

1. Introduction

The fluctuating wall pressures underneath a turbulent boundary layer are of interest both as a fundamental physical feature and for their practical implications as a cause of structural vibration (Blake 1986). Direct computation of a turbulent-boundary-layer flow at the Reynolds numbers of technological interest remains out of the question. Vibration predictions thus rely on empirical models of the pressure field (see, e.g. Graham 1997 and the references therein). Inevitably, such models have arbitrary features, due to the incompleteness and uncertainty in the measurements on which they are based. A simple, physically based model for the wall pressures would allow these features to be examined, as well as providing useful insight. Currently no such model exists.

For boundary-layer velocity spectra, however, the situation is different. Here, Perry and co-workers have developed the 'attached-eddy model', on the basis of ideas initially introduced by Townsend (1976). Townsend proposed that unsteady motions in the logarithmic region of a turbulent boundary layer arise from an ensemble of

† Present address: Department of Naval Architecture and Ocean Engineering, Chungnam National University, 79 Daehangno, Daejeon 305-764, Korea.

‡ Email address for correspondence: wrg@eng.cam.ac.uk

self-similar eddies, which may be regarded as ‘attached’ to the wall in the sense that their length scale, λ say, is proportional to distance from the wall. Their velocity scale is u_τ , the skin-friction velocity.

Perry & Chong (1982) took this viewpoint and added the insight that the proposed eddies must, in the mean, be responsible for the steady velocity component. This allowed them to deduce the dependence of the eddy distribution’s probability density function ($\sim\lambda^{-1}$) and the number of eddies per unit area ($\sim\lambda^{-2}$). They suggested that the latter quadratic decrease could be explained by a hierarchical model, whereby eddies grew in size, then either paired or died. They also, however, noted that this viewpoint was inconsistent with their kinematical modelling, which showed that growth in an individual eddy’s height was accompanied by a decrease in its breadth; the postulated circulation-doubling pairing does not provide a means of regaining the original eddy shape. Finally, they raised the possibility that attached eddies persist outside the logarithmic layer into the ‘defect-law’ region.

Perry, Henbest & Chong (1986) developed the model further, considering a range of candidate eddy shapes and showing how the probability density function could be weighted so that geometrically similar attached eddies could account for the logarithmic and defect-law velocity profiles. They also calculated the turbulence velocity spectra that would be expected on the basis of the postulated eddy distribution and found good agreement with measurements taken in zero-pressure-gradient boundary layers. Similar comparisons by Nickels *et al.* (2007), based on more recent data, also provide strong support for the attached-eddy viewpoint.

When applied to adverse-pressure-gradient and non-equilibrium boundary layers, however, the model was less successful. This observation stimulated the development of an extension, the ‘wall-wake’ form (Perry & Marusic 1995; Marusic & Perry 1995), which includes an additional population of detached eddies towards the edge of the boundary layer. Their influence, relative to that of the attached eddies, becomes noticeable high up in zero-pressure-gradient boundary layers, and can dominate for adverse-pressure-gradient and/or non-equilibrium conditions.

Plausible empirical support for the attached-eddy model came initially from smoke-flow-visualization experiments carried out by Head & Bandyopadhyay (1981). More recently, the advent of particle image velocimetry has enabled field measurements which, when carefully analysed, provide convincing evidence of the postulated flow structures (Adrian, Meinhard & Tomkins 2000; Hutchins, Hambleton & Marusic 2005; Hambleton, Hutchins & Marusic 2006). These studies also show that the eddies tend to occur in streamwise-oriented ‘packets’, associated with which are long ‘streaks’ of low-momentum fluid. Such streaks can extend further than 20 boundary-layer thicknesses (Hutchins & Marusic 2007), and modification of the attached-eddy model to take account of them improves its predictions of long-range correlation levels (Marusic 2001).

A more complete survey of current thinking on the structure of turbulent-boundary-layer flows can be found in the review paper by Adrian (2007). A recent direct-numerical-simulation study, by Wu & Moin (2009), is also relevant, in that it provides the first computational evidence for the presence of attached eddies in a fully turbulent regime.

Attempts to apply structure-based modelling to the wall-pressure spectrum have been rare; we have only found the work of Townsend (1976) and Witting (1986). Townsend considered a Gaussian eddy, of a single scale only, and restricted himself to a qualitative topological comparison with experimental results for the two-dimensional spatial correlation field (Bull 1967). Witting (1986) appears not to have been familiar

with the attached-eddy hypothesis, and instead derived a formulation based on an ensemble of dipoles, distributed over a range of heights in the boundary layer. This approach does not allow the probability density function of the distribution to be determined via the mean velocity profile, and Witting simply assumed it to be uniform. Nonetheless, like Townsend, he found good qualitative agreement with Bull's correlation measurements, albeit with significantly more rapid decay away from the central peak.

In summary, wall-pressure field modelling based on partially developed 'coherent structure' ideas has produced encouraging results, whereas an established form of these ideas, the attached-eddy model, has proved successful with regard to velocity spectra. The application of the attached-eddy model to the wall pressures is thus clearly worth pursuing, and is the topic of this paper. We begin, in §2, by calculating the wall-pressure field underneath a single, rectangular eddy. The scale integral, which expresses the wall spectrum in terms of weighted contributions from eddies of all sizes, is formulated in §3. Finally, the predictions of the model are tested in §4, against numerical and experimental data spanning a range of two decades in Reynolds number.

2. Surface pressures below a horseshoe vortex

As in the application of the attached-eddy model to velocity spectra, the overall wall-pressure spectrum will be formed from a superposition of individual eddy contributions. However, unlike the velocities, the pressures due to an eddy do not follow straightforwardly as soon as it is defined. Instead, it is necessary to solve the equations of motion for the fluid.

A further complication is the existence of two schools of thought on the single-eddy analysis. Dhanak & Dowling (1995) calculate the pressure field on the basis that the fluid surrounding the eddy is stationary at infinity. The pressures are then quadratic functions of the eddy vorticity and velocity fields. This nonlinearity means that the planned superposition of eddy pressure contributions is not strictly rigorous, even given the standard assumption of uncorrelated eddies. In practice, one might argue that it was nonetheless acceptable, if the mean velocity associated with other eddies were zero. This, however, is not the case; the attached-eddy model explicitly regards the mean contribution of all eddies as giving rise to the boundary-layer velocity profile.

The alternative approach is set out by Townsend (1976). Here the single-eddy pressure field is that due to the superposition of the eddy and the mean velocity profile. It is further assumed that the eddy velocity gradients are small in comparison with the mean shear, so the 'sources' in the Poisson equation for pressure may be linearized. This viewpoint regards the (mean) interaction of a given eddy with its peers as dominant; the quadratic 'self' pressures considered by Dhanak & Dowling (1995) are neglected, along with the fluctuating interaction components. As a corollary, it implies that the superposition of individual eddy pressure fields is legitimate.

The validity of Townsend's viewpoint depends on the size of the typical eddy velocities in comparison to the mean boundary-layer velocity. If, as he suggested, the former scale on the friction velocity, $u_\tau (= U_\infty \sqrt{c_f}/2$, in which U_∞ is the free-stream velocity and c_f is the wall skin-friction coefficient), then one expects it to be applicable for the high-Reynolds-number boundary layers of interest here. For this reason, it is the approach that we adopt.

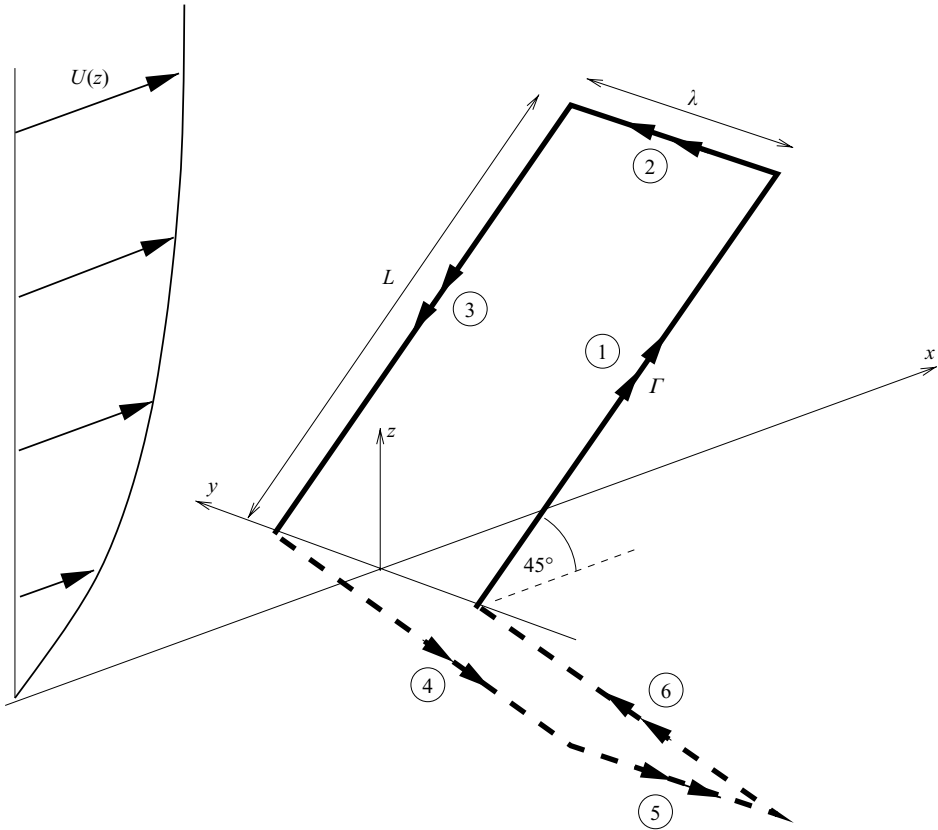


FIGURE 1. The horseshoe-vortex eddy representation, and its image in the x - y plane. Each straight-line element has circulation Γ , in the sense indicated by the double-headed arrows, and is labelled by a circled number.

In the following section, we define the eddy and give the Poisson equation for the pressure. In §2.2 we present a formal Green's function solution, in terms of the mean shear and the eddy velocities. Explicit expressions for the latter are given in §2.3; the mean shear is discussed in §2.4. The numerical method used to evaluate the Green's function integral is then described in §2.5, with sample results presented in §2.6. Finally, the associated wavenumber spectra are considered in §2.7.

2.1. Formulation

Following Perry *et al.* (1986), we specify our representative eddy in terms of its vorticity field. This consists of two straight 'legs', of length L and inclined at 45° to the mean flow, and a straight 'head', of length λ , perpendicular to the flow (figure 1). Each element of this 'horseshoe vortex' has uniform vorticity concentrated in a core of radius r_c , with corresponding circulation Γ . The associated flow vector is denoted by \mathbf{u} . The overall velocity field consists of the superposition of \mathbf{u} and the mean boundary-layer flow.

The origin of coordinates is located midway between the intersections of the horseshoe legs with the wall. The axes are chosen so that x is the streamwise direction and z is normal to the wall. The overall velocity vector is thus $(U + u)\mathbf{e}_x + v\mathbf{e}_y + w\mathbf{e}_z$, where $U(z)$ is the boundary-layer mean profile, (u, v, w) are the components of $\mathbf{u}(x, y, z)$ and $(\mathbf{e}_x, \mathbf{e}_y, \mathbf{e}_z)$ are the unit axis vectors.

The boundary layers that we seek to model here are high in Reynolds number, but still relatively low in Mach number. We therefore neglect the effects of viscosity and compressibility. The latter assumption is uncontentious, but the former could justifiably be questioned, and will be discussed further during the development of the analysis. Once accepted, they imply that the flow is described by the incompressible Euler equations, which take the form

$$\frac{\partial \mathbf{u}}{\partial t} + (U \mathbf{e}_x + \mathbf{u}) \cdot \nabla (U \mathbf{e}_x + \mathbf{u}) = -\frac{\nabla p}{\rho},$$

in which p is the flow pressure, ρ its density, and t represents time. The governing (Poisson) equation for the pressure field follows by taking the divergence; under the Townsend (1976) assumption that the mean shear dominates, it becomes

$$\nabla^2 p = -2\rho \frac{dU}{dz} \frac{\partial w}{\partial x}. \tag{2.1}$$

This equation is to be solved subject to the requirements that the pressure vanishes far from the eddy, and obeys the wall boundary condition:

$$\frac{\partial p}{\partial z} = 0. \tag{2.2}$$

Note that the inclusion of viscous effects would render this gradient non-zero, but the Poisson equation would still apply.

2.2. Solution for the surface pressures

Following Dhanak & Dowling (1995), we solve (2.1) via a Green's function approach. The required Green's function satisfies

$$\nabla'^2 G(\mathbf{x}'; \mathbf{x}) = \delta(\mathbf{x}' - \mathbf{x}) \tag{2.3}$$

and the boundary condition

$$\left. \frac{\partial G}{\partial z'} \right|_{z'=0} = 0. \tag{2.4}$$

(Here $\mathbf{x} = (x, y, z)$ and $\mathbf{x}' = (x', y', z')$ are position vectors in the flow half-space, $\delta(\mathbf{x}' - \mathbf{x})$ is a three-dimensional Dirac delta function, and the dash superscript on the 'del' operator means that its derivatives are with respect to the components of \mathbf{x}' .) The solution to (2.3) and (2.4) that vanishes at infinity is

$$G(\mathbf{x}'; \mathbf{x}) = -\frac{1}{4\pi} \left(\frac{1}{|\mathbf{x}' - \mathbf{x}|} + \frac{1}{|\mathbf{x}' - \mathbf{x}_I|} \right),$$

where $\mathbf{x}_I = (x, y, -z)$ is the image of \mathbf{x} associated with the wall plane. The pressure field may now be found from Green's theorem, which states that

$$\begin{aligned} \int_V [p(\mathbf{x}') \nabla'^2 G(\mathbf{x}'; \mathbf{x}) - G(\mathbf{x}'; \mathbf{x}) \nabla'^2 p(\mathbf{x}')] d^3 \mathbf{x}' \\ = \int_S [p(\mathbf{x}') \nabla' G(\mathbf{x}'; \mathbf{x}) - G(\mathbf{x}'; \mathbf{x}) \nabla' p(\mathbf{x}')] d^2 \mathbf{x}', \end{aligned} \tag{2.5}$$

where S is the surface bounding the domain V . On applying (2.5) to the half-space $z' > 0$, and employing (2.1)–(2.4), we have

$$p(\mathbf{x}) = -2\rho \int_{z'>0} G(\mathbf{x}'; \mathbf{x}) \frac{dU(z')}{dz'} \frac{\partial w(\mathbf{x}')}{\partial x'} d^3 \mathbf{x}'.$$

Had we included viscosity in our governing equations, this volume integral would have been supplemented by a surface integral involving the wall-normal pressure gradient. Howe (1989) considered the significance of this term and concluded that it only becomes relevant at length scales so large that compressibility effects are also important. Thus, in our context, its neglect is justifiable.

We conclude by restricting attention to points $\mathbf{x}_w = (x, y, 0)$ on the wall and integrating by parts, to obtain

$$p(\mathbf{x}_w) = \frac{\rho}{\pi} \int_{z' > 0} \frac{x' - x}{|\mathbf{x}' - \mathbf{x}_w|^3} \frac{dU(z')}{dz'} w(\mathbf{x}') d^3 \mathbf{x}'. \quad (2.6)$$

The motivation for the integration by parts is to obtain an integral which is more amenable to numerical evaluation. This exercise will be considered shortly; first, however, we must specify the integrand components dU/dz' and w .

2.3. The eddy velocity field

In principle, once the eddy's vorticity field $\boldsymbol{\omega}$ is defined, the associated velocities follow straightforwardly from the Biot–Savart integral. In practice, some difficulties arise. If the horseshoe elements in figure 1 are represented as line vortices, the velocity is singular at the corners. Some representation of the core structure is therefore required, but even the simplest forms one might consider do not admit exact analytical solutions. A plausible heuristic approach for slender elements is to de-singularize the Biot–Savart expression for the line element by multiplication with a modifying factor which corresponds to the exact Rankine core result for the infinite-length case. In Appendix A, we show that, subject to a slight correction, this method is asymptotically valid away from the ends of the element. Furthermore, we find that errors resulting from application of the corrected form at the ends as well are not great; in particular, they are likely to be negligible in comparison with other uncertainties, e.g. eddy geometry and core structure. On applying this approach to the eddy of figure 1, we obtain

$$w(x, y, z) = w_1 + w_2 + w_3 + w_4 + w_5 + w_6,$$

where the components w_1 – w_6 (arising, respectively, from the straight elements 1–3 and their images 4–6) are given in Appendix A.

2.4. The boundary-layer profile

The integral for the wall pressures, (2.6), requires the boundary-layer velocity gradient over the entire range in which both it and the wall-normal component of the eddy velocity are non-negligible. Therefore, given the range of eddy sizes postulated by the attached-eddy model, we must specify $U(z)$ throughout the boundary layer. In the log-law region, this is straightforward; there is broad agreement on the form of $U(z)$, and little variation in suggested values of its coefficients. Here we follow Nickels *et al.* (2007) and take

$$\frac{U}{u_\tau} = \frac{1}{\kappa} \log z^+ + A, \quad (2.7)$$

with $\kappa = 0.41$ and $A = 5.0$. The dimensionless variable z^+ is the coordinate z expressed in ‘wall units’, i.e. $z^+ = u_\tau z / \nu$, where ν is the fluid’s kinematic viscosity.

Below the logarithmic layer, the velocity profile is expected to be universal (when expressed in wall variables), but its form is less well established. Very near the wall, one expects $U/u_\tau = z^+$ (Young 1989). A more general empirical curve, formulated by

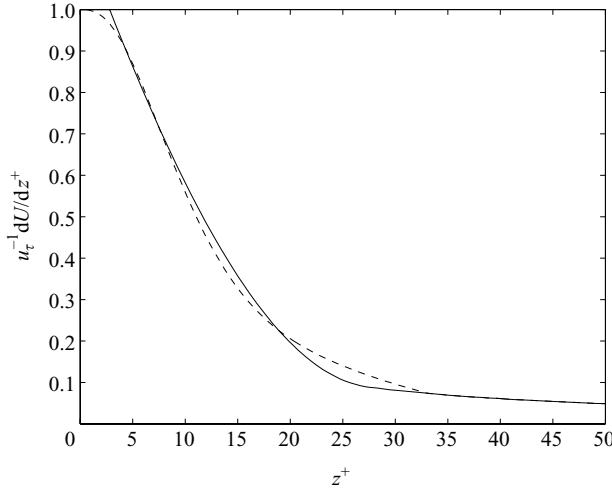


FIGURE 2. Comparison of expressions for the wall-region velocity gradient. The solid line (—), current (2.9); the dashed line (- -), Bull (2.8). Above $z^+ = 27.45$ and 33.2 the curves follow the log law $u_\tau^{-1}dU/dz^+ = 1/\kappa z^+$.

Bull (1969), is

$$\frac{1}{u_\tau} \frac{dU}{dz^+} = \left[1 + \frac{z^+}{4} + \frac{1}{2} \left(\frac{z^+}{4} \right)^2 + \frac{1}{1300} \left(\frac{z^+}{4} \right)^6 \right] e^{-z^+/4}, \tag{2.8}$$

valid for $z^+ \leq 33.2$. Here, for numerical reasons, we insist on the near-wall form $U/u_\tau = z^+$ for $z^+ \leq 2.8$. We then take

$$\frac{1}{u_\tau} \frac{dU}{dz^+} = 1 - \frac{z^+ - 2.8}{15.7} + 4.68 \times 10^{-4} (z^+ - 2.8)^{2.26}, \quad 2.8 < z^+ < 27.45. \tag{2.9}$$

The associated velocity profile is obviously continuous in value and gradient at $z^+ = 2.8$. It is also continuous with (2.7) in value, gradient and second derivative at $z^+ = 27.45$. The derivation of this expression is explained in Appendix B. It is compared with Bull’s form in figure 2.

Outside the logarithmic region the velocity profile is not expected to be universal. However, Young (1989) reports that a number of authors have achieved good fits to experimental data using expressions of the form

$$\frac{U}{u_\tau} = \frac{1}{\kappa} \log z^+ + A + \frac{B}{C\pi} \left[1 - \cos \left(C\pi \frac{z - z_2}{\delta} \right) \right], \tag{2.10}$$

where z_2 is the point at which the switch from the log law takes place, and δ is the boundary-layer thickness. This choice guarantees value and gradient continuity at $z = z_2$; the parameters B and C are set by the requirements that $U = U_\infty$ and $dU/dz = 0$ at $z = \delta$. In this work, we take $z_2 = 0.1\delta$ throughout. Appropriate values for B and C are given on a case-by-case basis in §4.

2.5. Numerical evaluation of the surface pressure field

The integral for the wall pressure, (2.6), was calculated via a straightforward quadrature on a Cartesian mesh, the contribution from each cell being taken as its volume multiplied by the integrand value at its centre. For practical implementation, this algorithm was split into a routine for the integral over x' and y' , in which the

velocity gradient does not appear, and a routine for the integral over z' . Numerical difficulties arising from the integrable singularity at $\mathbf{x}' = \mathbf{x}_w$ were avoided by starting the quadrature over z' at a non-zero lower limit, chosen so that dU/dz' was constant, and w linear in z' , below this limit. The missing part of the integral could then be evaluated analytically.

In each routine, the size of the cells was varied for numerical efficiency. For the integral over x' and y' , extra resolution was required at possible intersections between the integration plane and the horseshoe vortex legs or head. In the z' quadrature, the smallest cells were next to the wall and around the vortex head.

Accuracy requirements were set at the upper of 1% or 0.01, the latter applying to the dimensionless pressure

$$\tilde{p}(\mathbf{x}_w) = \frac{p(\mathbf{x}_w)}{\frac{1}{2} \rho u_\tau \frac{\Gamma}{\lambda}}.$$

Grid refinement and extension studies were carried out to ensure that these targets were met. Note that, in particular, this entails an upper limit on z' of four times the head height (assuming this to be less than the boundary-layer thickness), confirming the need for the defect-region velocity expression, (2.10), even for horseshoes with heads in the logarithmic region.

Finally, in the course of developing the calculation, we investigated the variation of the integrand contributions to $p(\mathbf{x}_w)$ with z' . This is significant because our eddy representation becomes questionable towards the feet, as the viscous sublayer is approached. We found that the contributions from these heights are small, unless \mathbf{x}_w itself is close to a foot. This observation, combined with our simple core model, suggests that there is a measure of arbitrariness in the details of the pressures around the feet. The large-scale structure of the field can, however, be regarded as robustly predicted.

2.6. Sample results

The wall pressures specified by (2.6) depend not only on position but also on the eddy parameters λ , L and r_c . In this section, we explore these dependencies.

First, we express the integral for the wall pressures in terms of dimensionless variables, viz.

$$\tilde{p} \left(\frac{x}{\lambda}, \frac{y}{\lambda}, \frac{L}{\lambda}, \frac{r_c}{\lambda}, \frac{u_\tau \lambda}{\nu} \right) = \frac{2}{\pi} \int_{z'>0} \lambda^2 \frac{x' - x}{|\mathbf{x}' - \mathbf{x}_w|^3} \left(\frac{\lambda}{u_\tau} \frac{dU}{dz'} \right) \frac{\lambda w}{\Gamma} \frac{d^3 \mathbf{x}'}{\lambda^3}.$$

The dimensionless eddy velocity field, $\lambda w/\Gamma$, is a function of \mathbf{x}'/λ , L/λ and r_c/λ , whereas the mean shear term depends on z'/λ and $u_\tau \lambda/\nu$. Hence, unlike its velocity field, the eddy's wall pressures cannot, in principle, take a universal form depending only on x/λ , y/λ , even if L/λ and r_c/λ are assumed constant. This observation has significant implications for our intended combination of contributions from eddies over many scales, and we therefore need to investigate the dependence on $u_\tau \lambda/\nu$ in practice (figure 3). We also consider the influence of the remaining dimensionless parameters, L/λ and r_c/λ (figures 4 and 5). In all these cases, the boundary layer is taken to have thickness $\delta = 3450\nu/u_\tau$ and defect-region velocity-profile constants $B = 7.34$, $C = 1.231$.

The essential conclusions from figures 3–5 are that the absolute size of the eddy has remarkably little effect on the dimensionless pressures; the aspect ratio is more important, and affects the large-scale topology of the pressure field; the influence of

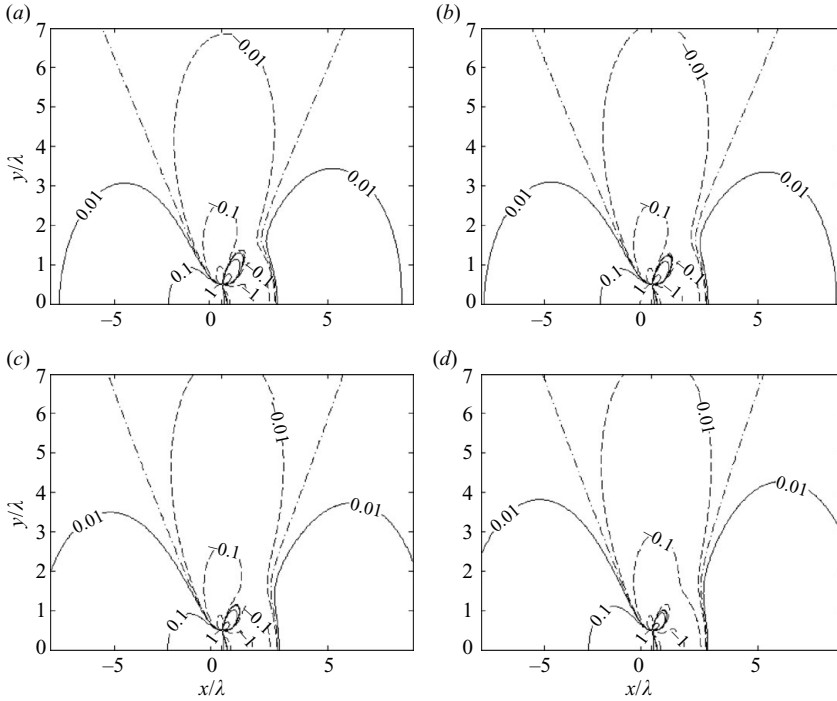


FIGURE 3. Eddy pressure field, $\tilde{p}(x/\lambda, y/\lambda)$, for $L/\lambda = \sqrt{2}$, $r_c/\lambda = 0.05$ and varying eddy size: (a) $u_\tau\lambda/\nu = 175$; (b) $u_\tau\lambda/\nu = 350$; (c) $u_\tau\lambda/\nu = 700$; (d) $u_\tau\lambda/\nu = 1400$. Lines: —, positive contour levels; - - -, zero contour level; - · - · -, negative contour levels.

the core size is limited to the regions around the feet of the eddy. The remainder of this section describes the plots in more detail.

Figure 3 shows pressure-field contours for eddies with $L/\lambda = \sqrt{2}$, $r_c/\lambda = 0.05$ and $u_\tau\lambda/\nu = 175, 350, 700, 1400$, placing the heads at $z = 0.05\delta, 0.1\delta$ (the top of our logarithmic region), $0.2\delta, 0.4\delta$, respectively. The first two fields are virtually identical, whereas the latter pair exhibit slight increases in outer lobe magnitudes with eddy size.

Figure 4 gives results for $u_\tau\lambda/\nu = 350$, $r_c/\lambda = 0.05$ and L/λ varying from 1 to $2\sqrt{2}$. Over this range, the main negative lobe grows, pushing the right-hand positive lobe away from the origin. The left-hand positive lobe changes less; in fact its expansion between $L/\lambda = \sqrt{2}$ and $2\sqrt{2}$ may be ascribable purely to the associated change in head height (to $z = 700\nu/u_\tau$; cf. figure 3c). Finally, a secondary positive lobe at the foot grows significantly with increasing L/λ .

Core-size variations (from 0.025λ to 0.2λ) for the eddy with $\lambda = 350\nu/u_\tau$ and $L = \sqrt{2}\lambda$ are shown in figure 5. Unsurprisingly, pressures distant from the eddy are unaffected; a close inspection of the contours around the foot reveals that the local peaks there are smoothed out as r_c increases.

2.7. The wavenumber spectrum

The superposition of eddy contributions to wall pressures will be in terms of wavenumber spectra. For this reason, we consider here the individual eddy spectrum, $|\tilde{P}(\tilde{k}_x, \tilde{k}_y)|^2$, where $\tilde{P}(\tilde{k}_x, \tilde{k}_y)$ is the Fourier transform of the (dimensionless) pressure

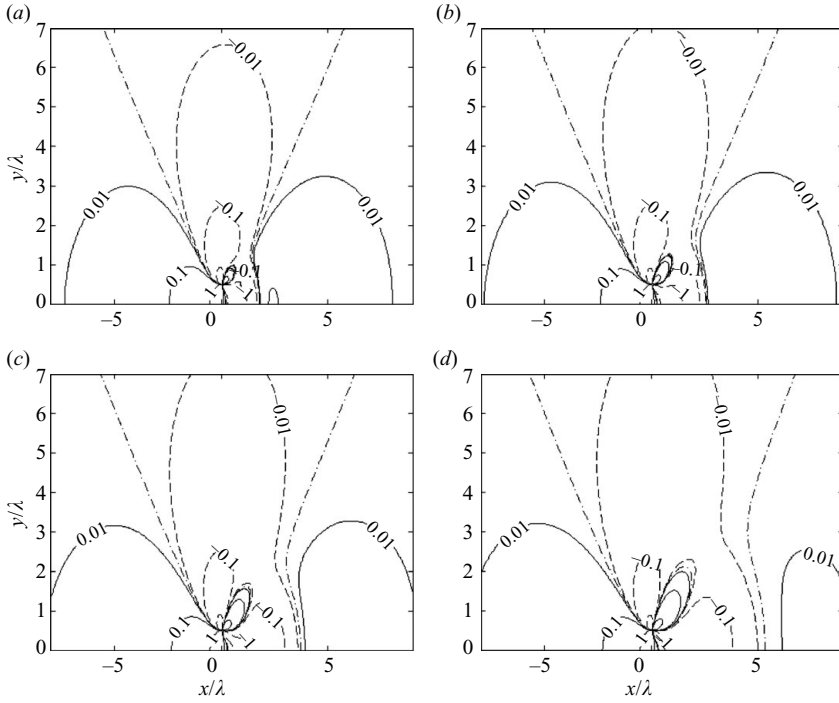


FIGURE 4. Eddy pressure field, $\tilde{p}(x/\lambda, y/\lambda)$, for $u_\tau\lambda/\nu = 350$, $r_c/\lambda = 0.05$ and varying aspect ratio: (a) $L/\lambda = 1$; (b) $L/\lambda = \sqrt{2}$; (c) $L/\lambda = 2$; (d) $L/\lambda = 2\sqrt{2}$. Lines: —, positive contour levels; - - -, zero contour level; · · ·, negative contour levels.

field:

$$\tilde{P}(\tilde{k}_x, \tilde{k}_y) = \int_{-\infty}^{\infty} \tilde{p}\left(\frac{x}{\lambda}, \frac{y}{\lambda}\right) e^{-i\tilde{k}_x x/\lambda} e^{-i\tilde{k}_y y/\lambda} d\left(\frac{x}{\lambda}\right) d\left(\frac{y}{\lambda}\right).$$

This quantity was estimated by applying a fast Fourier transform (FFT) algorithm to the pressure-field data, zero-padded to the nearest power of 2. Satisfactory high-wavenumber convergence in the spectrum was found with point spacing equal to the minimum of r_c and 0.05λ , corresponding to an upper (dimensionless) wavenumber limit of 62.8 or greater. Sufficient wavenumber resolution was obtained with limits of $-8, 9$ in x/λ and ± 7 in y/λ . Because of the zero padding, these give the same resolution in both \tilde{k}_x and \tilde{k}_y : 0.25.

Computational requirements were reduced in two ways. First, the symmetry of the pressure field in y was exploited. Second, a fourfold, bi-cubic interpolation scheme was used to provide the desired spatial resolution outside the region $-1.2 < x/\lambda < 2.0$, $y/\lambda < 1.6$. Inside this region, each required value was calculated directly.

Figure 6 shows the result of the spectrum calculation for the eddy common to figures 3–5, with $u_\tau\lambda/\nu = 350$, $L/\lambda = \sqrt{2}$ and $r_c/\lambda = 0.05$. The main peak lies on the \tilde{k}_x axis, but is offset from the origin. The dependence on \tilde{k}_y exhibits an oscillatory sidelobe structure, due to ‘interference’ between the two leg contributions to the pressure field.

In the previous section, we found that aspect-ratio variations affect the large-scale topology of the pressure field, and core-size variations affect the small-scale topology; these translate into influences on the low- and high-wavenumber regions, respectively, of the spectrum. In particular, the spectra corresponding to figure 4 (aspect ratio) show

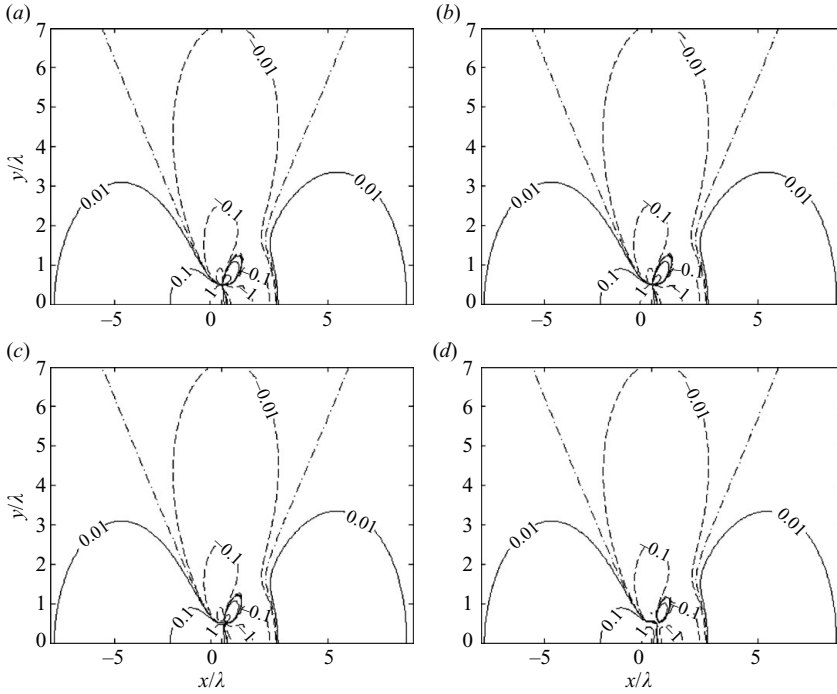


FIGURE 5. Eddy pressure field, $\tilde{p}(x/\lambda, y/\lambda)$, for $u_\tau \lambda/\nu = 350$, $L/\lambda = \sqrt{2}$ and varying core size: (a) $r_c/\lambda = 0.025$; (b) $r_c/\lambda = 0.05$; (c) $r_c/\lambda = 0.1$; (d) $r_c/\lambda = 0.2$. Lines: —, positive contour levels; - · -, zero contour level; --, negative contour levels.

differences only for $\tilde{k}_x, \tilde{k}_y < 5$, with levels on the \tilde{k}_x axis dropping as the streamwise length scale of the pressure field stretches, while those corresponding to figure 5 (core size) exhibit marked reductions in sidelobe levels with increasing r_c .

3. The overall surface pressure field

We now show how the attached-eddy model may be applied to obtain an expression for the wall-pressure spectrum in terms of an integral over contributions from eddies of differing scales. The approach taken differs slightly from that of Perry and co-workers by working throughout with the eddy ‘number density’ (the original Perry & Chong 1982 derivation quickly moves to the probability-density-function description), but is identical in principle. There are, however, two features of interest in our case.

The first has already been noted: it is not strictly possible to define a universal, dimensionless, eddy pressure field that is independent of eddy scale. The second is also a departure from self-similarity; it arises from the influence of eddies outside the logarithmic region on the wall pressures. That these are significant can be deduced from the narrow-band convection velocities reported for the wall-pressure field (Blake 1970), which typically range from around $0.83U_\infty$ to $0.6U_\infty$ over the frequency range where they are measurable. If we assume that the convection velocity is representative of the mean boundary-layer velocity at the eddy head, then the higher values certainly correspond to contributions from defect-layer eddies. (For the boundary-layer profile used in §2.6, the mean velocity at $z = 0.1\delta$ is $0.67U_\infty$, and it reaches $0.83U_\infty$ at $z = 0.4\delta$.) For this region, we follow Perry *et al.* (1986) in representing the relevant

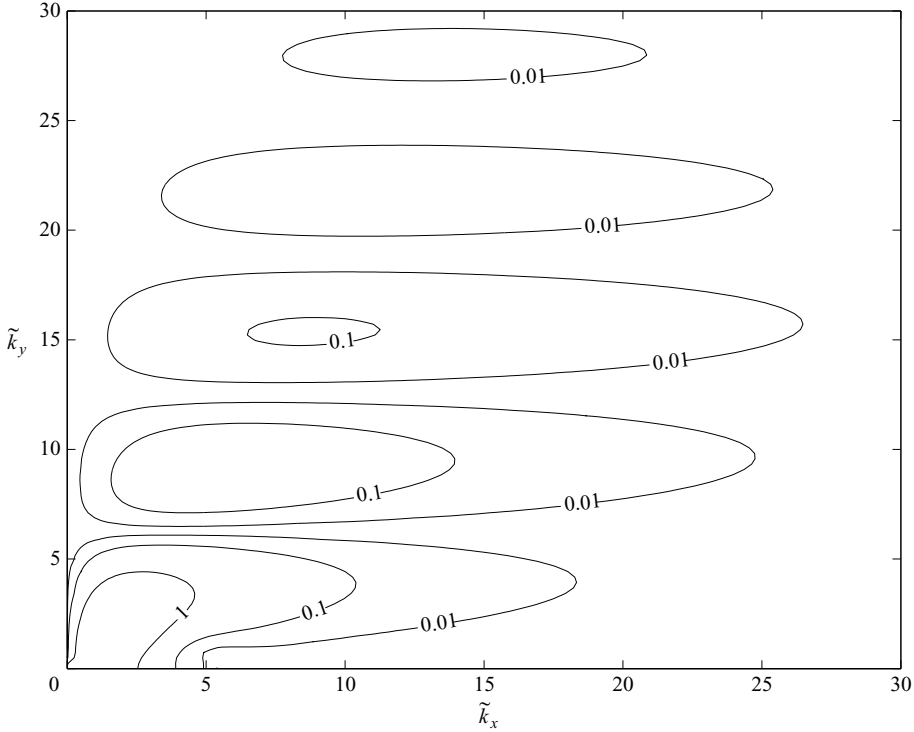


FIGURE 6. Eddy pressure spectrum, $|\tilde{P}(\tilde{k}_x, \tilde{k}_y)|^2$, for $u_\tau \lambda/\nu = 350$, $L/\lambda = \sqrt{2}$ and $r_c/\lambda = 0.05$.

eddies as still attached, but we do not assume that they are geometrically similar to their smaller counterparts. Instead we take up an alternative suggestion made by Perry & Chong (1982): that the departure from a logarithmic profile can be accounted for by changes in eddy shape. This approach still leads to a ‘scale integral’, which is derived in §3.1. The modifications necessary to include defect-layer contributions are discussed in §3.2, and numerical evaluation of the integral is considered in §3.3.

3.1. *Superposition of the eddy contributions*

To distinguish separate contributions, we introduce the nomenclature $p_e(x, y, \lambda)$ for the individual-eddy pressure field discussed in §2.2. Implicit in this description is an assumption that the core radius, r_c , and the leg length, L , are specified by the eddy width, λ . This issue will be discussed in §3.2.

Consider a distribution of eddies, represented by horseshoe vortices of a range of sizes and locations. The linearity of the pressure formulation, (2.6), implies that the wall pressure is the sum of individual contributions, i.e.

$$p(x, y) = \sum_m p_e(x - x_m, y - y_m, \lambda_m), \tag{3.1}$$

in which x_m, y_m and λ_m specify the location and size of the m th horseshoe.

Our interest is in the spatial spectrum

$$S(k_x, k_y) = \int_{-\infty}^{\infty} \int_{-\infty}^{\infty} R(r_x, r_y) e^{-ik_x r_x} e^{-ik_y r_y} dr_x dr_y, \tag{3.2}$$

where $R(r_x, r_y)$ is the ensemble-average pressure correlation function

$$R(r_x, r_y) = \overline{p(x, y)p(x + r_x, y + r_y)}.$$

This quantity cannot be directly extracted from our chosen representation of the boundary layer; instead we work with an alternative expression for the spectrum, which can be derived from its fundamental definition via generalized function theory, viz.

$$(2\pi)^2 \delta(k'_x - k_x) \delta(k'_y - k_y) S(k_x, k_y) = \overline{P(k_x, k_y) P^*(k'_x, k'_y)}, \quad (3.3)$$

where $\delta(\)$ is the Dirac delta function, and $P(k_x, k_y)$ is the Fourier transform of $p(x, y)$, defined in the same way as that for the spectrum, (3.2). On employing (3.1), it can be written as

$$P(k_x, k_y) = \sum_m P_e(k_x, k_y, \lambda_m) e^{-ik_x x_m} e^{-ik_y y_m}, \quad (3.4)$$

where $P_e(k_x, k_y, \lambda_m)$ is the transform of $p_e(x, y, \lambda_m)$. Our expression for the spectrum therefore becomes

$$(2\pi)^2 \delta(k'_x - k_x) \delta(k'_y - k_y) S(k_x, k_y) = \sum_m P_e(k_x, k_y, \lambda_m) P_e^*(k'_x, k'_y, \lambda_m) e^{i(k'_x - k_x)x_m} e^{i(k'_y - k_y)y_m}. \quad (3.5)$$

(Here one of the two summations over horseshoe contributions implied by (3.3) and (3.4) has been eliminated by the ensemble average, on the assumption that eddies are uncorrelated with one another. This is the standard approach; note, however, that it precludes any representation of the arrangement of eddies in packets.)

The next step is to replace the summation over eddies with an integral, reflecting the expected continuous distribution of sizes and locations. We define the *number density*, $n_e(\lambda)$, such that the expected number of eddies in the size range $\lambda_1 \leq \lambda \leq \lambda_2$ is $\int_{\lambda_1}^{\lambda_2} n_e(\lambda) d\lambda$, per unit of wall area. Then (3.5) becomes

$$(2\pi)^2 \delta(k'_x - k_x) \delta(k'_y - k_y) S(k_x, k_y) = \int_{\lambda_{min}}^{\lambda_{max}} \int_{-\infty}^{\infty} \int_{-\infty}^{\infty} n_e(\lambda) P_e(k_x, k_y, \lambda) \times P_e^*(k'_x, k'_y, \lambda) e^{i(k'_x - k_x)x_m} e^{i(k'_y - k_y)y_m} dx_m dy_m d\lambda.$$

The integrations over x_m and y_m yield delta functions, which can be eliminated by further integrations (of both sides) over k'_x and k'_y . The final result is

$$S(k_x, k_y) = \int_{\lambda_{min}}^{\lambda_{max}} n_e(\lambda) |P_e(k_x, k_y, \lambda)|^2 d\lambda, \quad (3.6)$$

where λ_{min} and λ_{max} are the sizes of the smallest and largest horseshoes, respectively. This is the *scale integral* for the wavenumber spectrum. As it is an average quantity, it requires no assumption beyond that of uniform probability for the spatial arrangement of our eddies. Their size distribution, however, must be specified, and this is the topic of §3.2.

Here, we conclude by stating the corresponding results for the one-dimensional wavenumber spectra defined by

$$S_x(k_x) = \int_{-\infty}^{\infty} R(r_x, 0) e^{-ik_x r_x} dr_x,$$

$$S_y(k_y) = \int_{-\infty}^{\infty} R(0, r_y) e^{-ik_y r_y} dr_y.$$

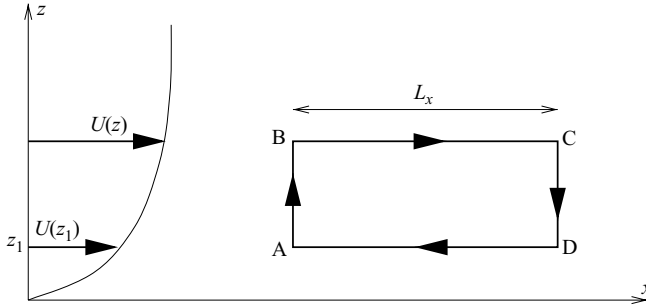


FIGURE 7. Notation for analysis linking eddy number density to streamwise velocity gradient.

A similar analysis to that above gives

$$S_x(k_x) = \int_{\lambda_{\min}}^{\lambda_{\max}} \int_{-\infty}^{\infty} n_e(\lambda) |P_{ex}(k_x, y, \lambda)|^2 dy d\lambda$$

with

$$P_{ex}(k_x, y, \lambda) = \int_{-\infty}^{\infty} p_e(x, y, \lambda) e^{-ik_x x} dx.$$

The corresponding expression for $S_y(k_y)$ can be deduced via appropriate variable exchanges.

3.2. The eddy distribution

Townsend’s attached-eddy hypothesis postulates a distribution of self-similar eddies with velocity scale u_τ . Perry and co-workers identified the horseshoe vortex as a candidate eddy structure and showed that the average size distribution could be inferred from the requirement that the eddies be responsible, in the mean, for the boundary-layer velocity profile. Here we apply this insight to deduce the form of our number-density function in, and then outside, the logarithmic region.

Consider the streamwise plane ABCD shown in figure 7. Under the usual boundary-layer assumptions, the mean circulation around this region is, by definition, $[U(z) - U(z_1)]L_x$. This quantity arises from the heads of the horseshoe vortices that cut the plane. To do so, a horseshoe of breadth λ must lie within a spanwise distance $\lambda/2$ either side of the plane and have head height $L/\sqrt{2}$ between z_1 and z . For the latter condition to be fulfilled, we require $\Lambda z_1 < \lambda < \Lambda z$, where $\Lambda = \sqrt{2}\lambda/L$ is a constant for our self-similar eddies. When this requirement is satisfied, the number of horseshoes with breadth between λ and $\lambda + d\lambda$ which cut the plane is $n_e(\lambda)d\lambda L_x \lambda$, each contributing circulation $\Gamma(\lambda)$. Equating the overall circulation with the integral of the horseshoe contributions then gives

$$U(z) - U(z_1) = \int_{\Lambda z_1}^{\Lambda z} n_e(\lambda) \Gamma(\lambda) \lambda d\lambda, \tag{3.7}$$

or

$$\frac{dU}{dz} = \Lambda^2 z n_e(\Lambda z) \Gamma(\Lambda z). \tag{3.8}$$

Now the assumed eddy scaling implies that $\Gamma(\lambda) \sim u_\tau \lambda$, so we require

$$n_e(\lambda) = \frac{N_e}{\lambda^3}$$

(with N_e constant) if (3.8) is to reproduce the log law, $dU/dz \propto 1/z$.

Such a form for the number density implies that the number of horseshoes in a finite (percentage) range around a given scale reduces by a factor of four each time that scale doubles. This led Perry & Chong (1982) to propose that, in the process of growing to the larger scale, half the vortices ‘die’, and half ‘pair’, i.e. merge with similar partners, leading to a doubling in eddy circulation. As the pairing vortices must, more-or-less, line up with one another, we shall refer to this process as ‘streamwise pairing’. Perry & Chong (1982) noted that this view, combined with horseshoe elongation during growth, is inconsistent with the self-similarity assumption, but did not pursue the matter. We suggest that the difficulty could be resolved by postulating a second, ‘spanwise’, pairing process instead of vortex ‘deaths’. Vortices pairing spanwise would start side-by-side, and would join via cancellation of their adjacent legs. This process would be circulation conserving, hence not contravening the required scaling, and would provide a mechanism for spanwise growth.

Above the logarithmic region, we make the physically plausible assumption that the joining and merging processes continue, but that the vortex stretching is increasingly inhibited as the edge of the boundary layer is approached. This implies that the number density and circulation depend on λ as previously, but that the horseshoes are no longer geometrically similar, i.e. Λ is now a function of λ . In this case (3.7) still holds, but

$$\frac{dU}{dz} = (\Lambda z)^2 n_e(\Lambda z) \Gamma(\Lambda z) \left[\frac{1}{z} + \frac{1}{\Lambda} \frac{d\Lambda}{dz} \right].$$

Our defect region velocity profile, (2.10), is then matched when

$$\log \frac{\Lambda}{\Lambda_0} = \frac{\kappa B}{C\pi} \left[1 - \cos \left(C\pi \frac{z - z_2}{\delta} \right) \right],$$

where Λ_0 is the constant value of Λ applicable in the logarithmic region.

This definition of the eddy distribution satisfies our assumption that the leg length, L , is a function of λ . However, we also required the core radius to be defined by λ , and a form for this dependence is not easily obtainable from arguments *a priori*. The most straightforward assumption is that r_c is proportional to λ , and this is the approach taken by Perry *et al.* (1986). It has no strong physical justification; although one would expect core sizes to increase because of the postulated streamwise merging, they would not necessarily remain proportional to λ , and in any case the stretching process would oppose this tendency (for the legs, at least). However, any significant departure from proportionality would imply the presence of another relevant length scale, and this is not observed empirically. Alternatively, recall that it is the low-amplitude, high-wavenumber regions of an eddy’s pressure spectrum that are affected by r_c , and these will only contribute significantly to the scale integral at a given wavenumber, k_x say, when there are no higher amplitude contributions arising from the lower $k_x \lambda$ regions of smaller eddies’ spectra. On the basis of these arguments, then, we fix r_c at 0.05λ .

3.3. Numerical evaluation of the scale integral

We have already noted that the wall-pressure field is not self-similar. However, to inform the following discussion, we consider first how the scale integral would be evaluated if it were. In this case, the eddy pressure field could be expressed as

$$p_e = \frac{1}{2} \rho u_\tau \frac{\Gamma}{\lambda} \tilde{p}_e \left(\frac{x}{\lambda}, \frac{y}{\lambda} \right)$$

(cf. §2.6), and its Fourier transform as

$$P_e = \frac{1}{2} \rho u_\tau \Gamma \lambda \tilde{P}_e(k_x \lambda, k_y \lambda),$$

where $\tilde{P}_e(\tilde{k}_x, \tilde{k}_y)$ is the Fourier transform of $\tilde{p}_e(x/\lambda, y/\lambda)$ with respect to its arguments. Noting that $\Gamma \sim u_\tau \lambda$, the scale integral, (3.6), would then become

$$S(k_x, k_y) \sim \left(\frac{1}{2} \rho u_\tau^2 \right)^2 \int_{\lambda_{min}}^{\lambda_{max}} \lambda |\tilde{P}_e(k_x \lambda, k_y \lambda)|^2 d\lambda. \quad (3.9)$$

Thus, for any given (k_x, k_y) , we would evaluate a line integral proceeding along a fixed ratio of the dimensionless wavenumbers \tilde{k}_x, \tilde{k}_y in the ‘universal’ spectrum $|\tilde{P}_e(\tilde{k}_x, \tilde{k}_y)|^2$. Crucially, the latter need only be evaluated once.

In the absence of self-similarity, however, we have to consider direct evaluation of (3.6), which requires $P_e(k_x, k_y, \lambda)$ to be computed for every value of λ in whichever quadrature is chosen. This, unfortunately, turns out to be numerically prohibitive. We must therefore assess the importance of departures from self-similarity.

As we have seen, such departures arise from two sources. The first is the contribution of all regions of the boundary layer to the integral for eddy pressures, via the mean-shear term dU/dz' , and the second is the variation in eddy aspect ratio required outside the logarithmic region. The former, however, was found in §2.6 to have a very weak effect on the surface pressure field, and we therefore neglect it. This then implies that the contribution to the scale integral from eddies in the logarithmic region can be expressed in the universal form, (3.9).

The dependence of the surface pressures on aspect ratio is more important. The variation of aspect ratio with scale is, however, rather gradual, compared to the other components influencing the integrand: $\lambda, k_x \lambda$ and $k_y \lambda$. We can therefore split the scale range into a small number of contributions, within each of which the aspect ratio may be considered fixed, and the required (dimensionless) spectrum universal. This makes the problem numerically tractable.

The next consideration is the choice of limits for the scale integral. It is natural to take the lower, λ_{min} , as corresponding to the base of the logarithmic region ($z^+ = 27.45$ here). This scale, however, is rather small at high Reynolds numbers, meaning that it is difficult to resolve in either measurements or computations. The value 27.45 should therefore be regarded as a lower limit, only applicable in the absence of any high-wavenumber filtering.

The upper limit for the scale integral is less easily defined. Although Perry and co-workers’ early modelling assumed the largest attached eddies to have their heads at the edge of the boundary layer, the later ‘wall-wake’ development considers structures at this height to be detached. Direct support for this viewpoint is provided by the recent experiments of Hutchins *et al.* (2005) and Hambleton *et al.* (2006). In our case, initial calculations with attached eddies all the way to the boundary-layer edge produced poor agreement with the test data sets described in §4. A reduction in maximum head height thus seems justified, on both physical and empirical grounds.

Guidance for an appropriate value was taken from the measured narrow-band convection velocities discussed earlier. Although these are average values, they do provide some indication of the heights of the structures that contribute to the wall pressures. The largest observed convection velocities correspond to the mean boundary-layer velocity at about 0.4δ , and λ_{max} was thus set to place the largest eddies’ heads at this height. (Note, in passing, that this is around the beginning of

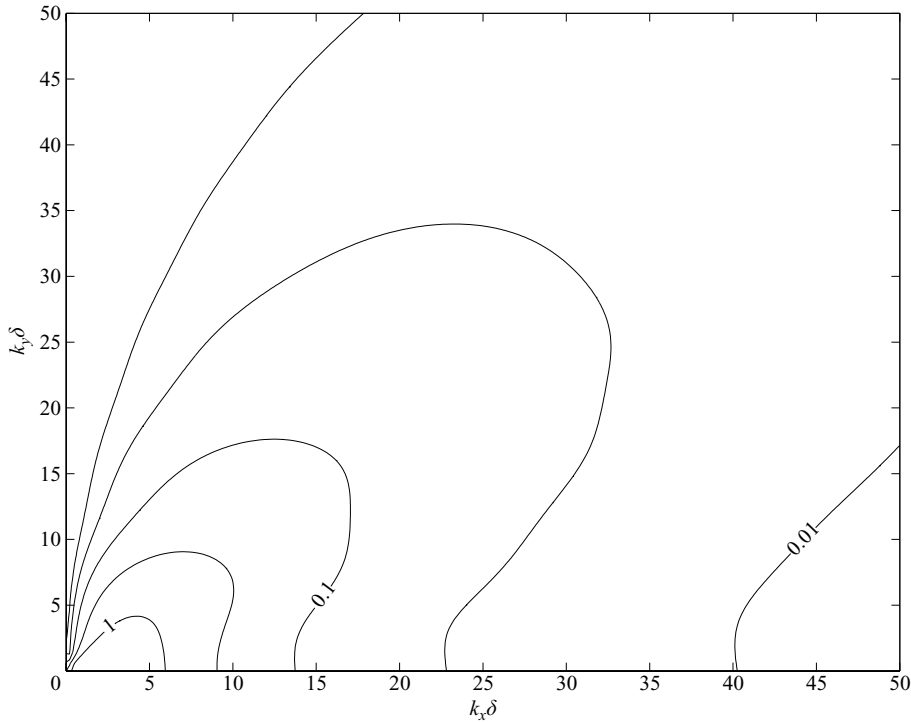


FIGURE 8. Example two-dimensional wavenumber spectrum for the wall pressures, calculated from the scale integral, (3.6). Note that contour level values are relative, not absolute.

the intermittent region, Young 1989, nonetheless it should be regarded as a physically allowable, rather than essential, choice, and could therefore be varied.) On the same basis, we neglect potential contributions from detached structures high up in the boundary layer.

Specific details of the numerical implementation are as follows. Within each quasi-universal scale range, the integration over scale is carried out with Simpson's rule, using bi-linear interpolation to obtain the spectrum values at the required wavenumber. The resolution of the quadrature is dictated by the number of points available in the 'universal' spectrum. The number of scale ranges outside the logarithmic region is five, with exponential spacing in z (i.e. the boundaries are at $z/\delta = 0.1, 0.132, 0.174, 0.230, 0.303$ and 0.4). The corresponding values of λ and L depend on the boundary-layer parameters and the aspect ratio chosen for the logarithmic region eddies. For the example used previously, with boundary-layer parameters $\delta = 3450\nu/u_\tau$, $B = 7.34$, $C = 1.231$, and with $L = \sqrt{2}\lambda$ in the logarithmic region, we have $\lambda/\delta = 0.1, 0.133, 0.180, 0.253, 0.381$ and 0.639 at the scale-range boundaries. These values are averaged to find λ/δ for the 'universal' eddies: $0.116, 0.156, 0.216, 0.317$ and 0.510 . Finally, the associated values of L/λ are $1.412, 1.391, 1.330, 1.203$ and 0.992 .

The result of this process, for eddies with $r_c = 0.05\lambda$ and a lower limit $\lambda_{min} = 27.45\nu/u_\tau$, is shown in figure 8. Note that, as the overall multiplying factor for the scale integral is unknown, the absolute amplitude is arbitrary. The resolution of the contour levels is twice that used for the individual eddy spectrum of figure 6. Wavenumbers are non-dimensionalized on the boundary-layer thickness.

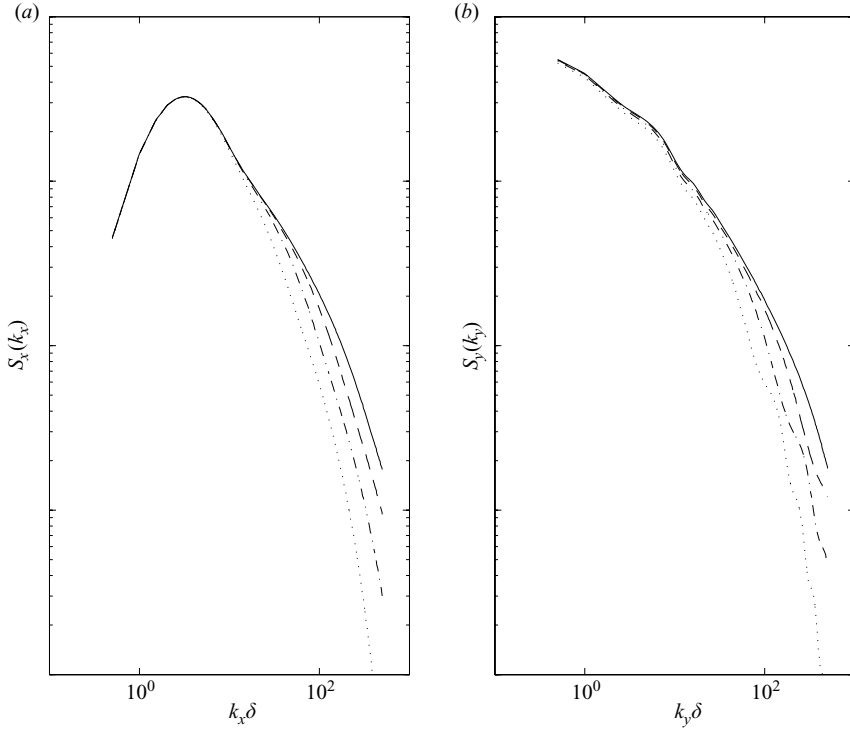


FIGURE 9. One-dimensional wavenumber spectra calculated from scale integrals with differing lower limits: (a) streamwise spectrum; (b) spanwise spectrum. Lines: —, $u_\tau \lambda_{min}/\nu = 25$; - -, $u_\tau \lambda_{min}/\nu = 50$; - · -, $u_\tau \lambda_{min}/\nu = 100$; · · ·, $u_\tau \lambda_{min}/\nu = 200$. Vertical scale is logarithmic and spans four decades.

The overall shape of the spectrum contours is clearly derived from that of the main peak in the eddy spectra. However, the additional lobes observed with increases in k_y have been removed by the smoothing effect of the scale integral. The broadening of the peak arises from the stretching of the eddy spectra – functions of $k_x \lambda$, $k_y \lambda$ – in the $k_x \delta$, $k_y \delta$ plane.

Given the possible increase in the lower scale-integral limit that may be necessary to account for wavenumber filtering, it is also worth considering the effect of this parameter on the calculated spectrum. Figure 9 shows the one-dimensional spectra for our example case, with $u_\tau \lambda_{min}/\nu = 25, 50, 100$ and 200. The effect of increasing λ_{min} is, as one would expect, to attenuate the spectra at higher wavenumbers. For the largest value, the associated wavenumber ($2\pi/\lambda_{min}$) is about $100/\delta$, at which point the streamwise spectrum has been attenuated approximately fourfold and the spanwise approximately threefold.

Having described the numerical implementation of the attached-eddy surface pressure model, we are now in a position to compare its predictions with results found in practice. This is the subject of §4.

4. Comparison with experimental and computational data

The assessment of our model's predictions is somewhat complicated by their 'broadband' nature; many of the processed results reported in the literature

concentrate on individual frequency components of the spatial correlation function. We therefore need to consider either older data sets, or ones where the original time histories are available. We have identified four such sets.

The first, that of Bull (1967), is due to one of the earliest substantial studies in the field. Bull used 0.74 mm flush-mounted transducers to measure the pressure fluctuations under boundary layers with free-stream Mach numbers of 0.3 and 0.5, and thicknesses ranging from 11 mm to 36 mm. The study is notable for its measurements of off-axis, in addition to the usual streamwise and spanwise, correlations. However, doubts as to its accuracy were expressed by Blake (1970), who employed 0.79 mm pinholes with thicker boundary layers to improve transducer resolution and found faster decay in correlation with distance. For this reason, we use Blake's data (Mach number and boundary-layer thickness ranges 0.06–0.15 and 42–46 mm, respectively) in preference, where possible.

A more recent experimental data set, for which time histories are available, was collected by NASA, Boeing and ANTK Tupolev in the course of an extensive set of flight tests on a Tu-144 aircraft (Rizzi, Rackl & Andrianov 2000). Although most of the flights were at supersonic speeds, some data at a Mach number of 0.58 are available. Boundary-layer thicknesses were not measured, but would typically be a factor of 10 greater than those of Bull and Blake.

Finally, we have also obtained a numerical data set: the large-eddy simulation (LES) carried out by Singer (1996*a*). This calculation is for incompressible flow, at a Reynolds number (based on displacement thickness and free-stream velocity) of 3500. This places it at the extreme lower end of our test-case range; for comparison, the Blake, Bull and Tu-144LL values are roughly 2×10^4 , 3×10^4 and 3×10^5 , respectively.

In the following section, we describe the data sets in more detail and consider how they may be compared to the model predictions. The comparisons themselves are split between two sections: the first (§4.2) representing on-axis (i.e. streamwise and spanwise) and the second (§4.3) off-axis results. The implications are discussed in §4.4.

4.1. *The data sets*

4.1.1. *Bull's measurements*

Bull's experiments were performed in a 225×150 mm wind tunnel, with up to ten pressure transducers at spacings ranging from 2.5 mm to 63 mm. In only one case were off-axis correlations, at 30° and 60° , measured in addition to streamwise and spanwise; here the free-stream Mach number was 0.3 and the boundary-layer displacement thickness was 3.8 mm. (Other relevant parameters are given in table 1. From these, we note that the 0.74 mm transducer diameter corresponds to $162\nu/u_\tau$, implying that contributions from the smallest eddies are filtered out.) Using the measurements for this case, Bull drew a contour plot of the two-dimensional correlation field, and this is the subject of our comparison.

On the basis that the dominant length scale of an eddy's wall-pressure field is the leg spacing, λ , the scale integral for the wavenumber spectrum was calculated with a lower limit set by the transducer diameter, i.e. $\lambda_{\min} = 162\nu/u_\tau$. The predicted correlation map was then found via inverse Fourier transform. Following a resolution study, the spectrum was calculated up to $k_x\delta, k_y\delta = 500$, with resolution 0.5. After zero-padding to the next highest power of 2 and carrying out the inverse transform, correlation values up to $r_x/\delta, r_y/\delta = 6.28$ were obtained, at a resolution of 0.00613.

| Set | U_∞ (m s ⁻¹) | c_f | u_τ (m s ⁻¹) | ν (m ² s ⁻¹) | $u_\tau \delta / \nu$ | B | C |
|----------|---------------------------------|-----------------------|-------------------------------|---|-----------------------|-------|-------|
| Singer | N/A | 3.33×10^{-3} | N/A | N/A | 1000 | 5.59 | 1.271 |
| Blake | 37.9 | 2.45×10^{-3} | 1.33 | 1.65×10^{-5} | 3450 | 7.34 | 1.231 |
| Bull | 100 | 2.14×10^{-3} | 3.28 | 1.50×10^{-5} | 6600 | 8.12 | 1.219 |
| Tu-144LL | 182 | 1.33×10^{-3} | 4.69 | 2.13×10^{-5} | 106,000 | 10.63 | 1.193 |

TABLE 1. Boundary-layer parameters for the comparison data sets.

4.1.2. Blake's measurements

The wind-tunnel facility used by Blake had a 375 mm square cross-section, and transducer spacings ranged from 7.9 mm to 127 mm. Only streamwise and spanwise correlations are reported, for Mach numbers of 0.084 and 0.111. Of these two data sets, the latter extends to a slightly smaller (dimensionless) streamwise separation, and is therefore the one we compare against. It has displacement thickness 7.2 mm; other relevant parameters are given in table 1. The comparison is based on streamwise and spanwise correlations, with calculated values being obtained via the one-dimensional analogue of the process described in §4.1.1. Blake's transducer diameter is $64\nu/u_\tau$, so λ_{min} was set to this value for the scale integral. The extents and resolutions of the calculated correlations are unchanged.

4.1.3. The Tu-144LL measurements

As the current model seeks to represent incompressible boundary layers, only the lowest speed, $M = 0.56$, data were inspected. Among these, a number of pressure transducer spectra were found to exhibit extraneous tonal noise. After excluding transducer groups with any members affected by this problem, we are left with measurements taken 48.4 m from the nose (window blank 7) at altitude 4970 m (flight 19).

Our outer-region velocity profile requires knowledge of the friction velocity u_τ (or, equivalently, the free-stream velocity and the skin-friction coefficient), the kinematic viscosity and the boundary-layer thickness. Of this required information, only the free-stream velocity, $U_\infty = 182$ m s⁻¹, is available directly. The remaining parameters were estimated from standard expressions (see Appendix C for details).

The relative locations of the pressure measurements are shown in figure 10. Also indicated is a free stream, U_∞ , at an angle to the transducer axes, due to the aircraft incidence and possible local flow distortion around the fuselage. This angle was estimated from the projected convection velocities implied by the time lag to maximum correlation between the extreme near-streamwise and near-spanwise transducer pairs. The result was 7.6° , which compares very favourably with the 7.7° incidence recorded by the aircraft's flight-data system. The corresponding overall convection velocity was calculated at 71 % of free stream, in excellent agreement with expectation.

Finally, we must consider the wavenumber filtering issue. The effective transducer size, in this context, is given by Rizzi *et al.* (2000) as 7.72 mm. A complicating factor, however, is the use of anti-alias (low-pass) filters, set at 11.2 kHz, in the data collection. The transducer size can only be used to determine the scale cutoff if its filtering effect is more stringent than the anti-aliasing. The eddies whose contributions would be attenuated by the latter are identified by linking the peak in the eddy spectrum (at around $k_x \lambda = 2$) to the convective wavenumber, ω/U_c (where U_c is the mean convection velocity), at 11.2 kHz. Taking $U_c = 0.7U_\infty$, one obtains $\lambda \simeq 3.6$ mm, which

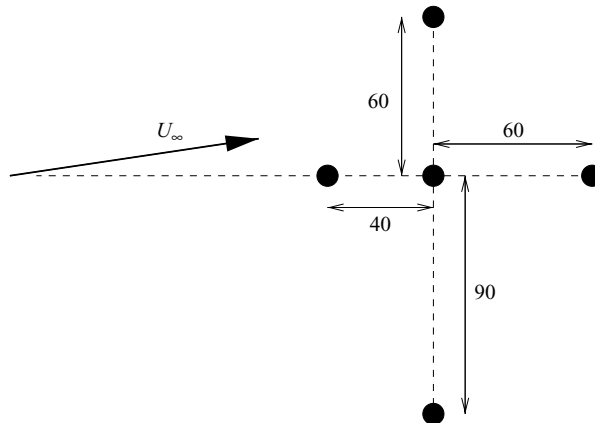


FIGURE 10. Pressure transducer locations in window blank 7 of the Tu-144LL flight-test aeroplane. Dimensions are in mm.

is smaller than the effective transducer diameter. The lower limit of the scale integral was thus set to 7.72 mm, i.e. $1700\nu/u_\tau$.

The comparison between data and predictions is again carried out via correlations. For the measurements, these were calculated using software supplied with the raw data. Predicted values were obtained by interpolation from a two-dimensional field calculated in the same way as described in §4.1.1, with the same spatial resolution. Although all the measurements are off-axis to some extent, results from the nominally streamwise and spanwise separations are considered with the on-axis results from the other data sets.

4.1.4. Singer's large-eddy simulation

Singer's calculation was carried out with a Fourier–Chebyshev pseudo-spectral code, periodicity being enforced in the spanwise and streamwise directions. (A coordinate transformation, due to Spalart 1988, was employed to allow the spectral representation in the latter.) The free-stream velocity and boundary-layer displacement thickness (δ^*) were chosen as reference variables, and the corresponding Reynolds number was set to 3500. The streamwise and spanwise extents of the computational domain were $44.88\delta^*$ and $14.28\delta^*$ respectively, with either 96×96 grid points ('coarse') or 192×128 ('fine'). The resulting friction velocity was $0.041U_\infty$, and the mean velocity reached $0.99U_\infty$ at a height $1000\nu/u_\tau$, approximately. Taken together with the imposed Reynolds number, these figures imply that $\delta/\delta^* = 7.0$.

Wavenumber spectra were estimated by averaging FFTs of the fine-grid wall-pressure field, with its (spatial) mean value subtracted. Each field was first Hanning-windowed and zero-padded to 256 points (streamwise) by 512 (spanwise; this value was chosen to achieve wavenumber resolution comparable to the streamwise direction). The resulting spectra are thus defined up to $k_x\delta = 94$, $k_y\delta = 197$, with resolutions of 0.74 and 0.77.

The length of available data is 2550 time steps of $0.2\delta^*/U_\infty$. However, correlation between pressure fields at nearby times means that the useful number of FFTs for averaging is lower; beyond 510, no improvement in convergence was observed for the two-dimensional spectrum, even though the estimate, as will be seen, clearly demonstrates the effects of statistical uncertainty. More realizations could, however, be used for the one-dimensional spectra, as each time step provides multiple samples

whose correlation decreases with their spacing. In practice, we found that 20 streamwise or spanwise lines per field, corresponding to an average over 10 200 FFTs, was the useful limit. An improvement in spectral convergence over the 510 FFT averages was evident for both streamwise and spanwise spectra, but was particularly marked for the former.

As the spectra calculated from the theoretical model have arbitrary absolute levels, some form of normalization is also required. The LES spectra were therefore divided by their integrated values, estimated using trapezoidal quadrature. ‘De-aliasing’ (i.e. filtering out of high-wavenumber components) in the LES algorithm cuts off the spectra above $k_x\delta = 61.76$, $k_y\delta = 126.26$; hence, only data for lower wavenumbers were used in the integrations. The same ranges were employed in the corresponding normalizations for the theoretical spectra.

To identify the eddies that are attenuated by the de-aliasing, it is necessary to consider both streamwise and spanwise length scales in the eddy pressure field. Here, we argue that the former is significantly larger than the latter, which is given by λ . Thus, the spanwise de-aliasing dominates, and eddies with $\lambda < 0.050\delta$ will have their contributions eliminated. A lower limit of $\lambda = 50\nu/u_\tau$ was therefore used in the scale integral.

4.2. On-axis results

Here we present comparisons between one-dimensional data and the predictions of our model, the latter for three different base-eddy aspect ratios: $L = \lambda$, $L = 2^{1/4}\lambda$ and $L = \sqrt{2}\lambda$ (i.e. $\Lambda_0 = \sqrt{2}$, $2^{1/4}$ and 1). The data sets are arranged in order of increasing Reynolds number.

4.2.1. Singer’s LES data

As noted previously, the absolute level of our theoretical predictions is arbitrary. We do, however, have the result that

$$\overline{p^2} = \frac{1}{2\pi} \int_{-\infty}^{\infty} S_x(k_x) dk_x, \quad (4.1)$$

so the dimensionless function $S_x(k_x)/\overline{p^2}\delta$ can be obtained by normalizing the spectrum with its integrated value. This quantity, and its spanwise counterpart, are plotted in figure 11.

As one would expect, the predictions for different aspect ratios converge at higher wavenumbers, showing excellent agreement with the numerical results for the spanwise case, and slightly higher levels for the streamwise. At intermediate wavenumbers, where the spectra exhibit inverse-wavenumber dependence, there is good agreement with the LES data in both. Here the aspect ratio still has little effect on the predicted streamwise spectrum, but there are some differences in the spanwise direction, with the $L = 2^{1/4}\lambda$ curve matching best. Finally, the low-wavenumber predictions decrease with increasing leg length; the spanwise still match the LES data well, but the streamwise diverge at the very lowest values. Again, the $L = 2^{1/4}\lambda$ calculation appears to give the best overall agreement.

4.2.2. Blake’s wind tunnel data

In this case, the arbitrariness in the absolute level of the theoretical predictions is straightforwardly dealt with by considering cross-correlations normalized on their value at zero separation (i.e. p^2). Figure 12 compares the predicted and measured data on this basis. (Note that one experimental data point, at $r_x = 2.4\delta$, has been

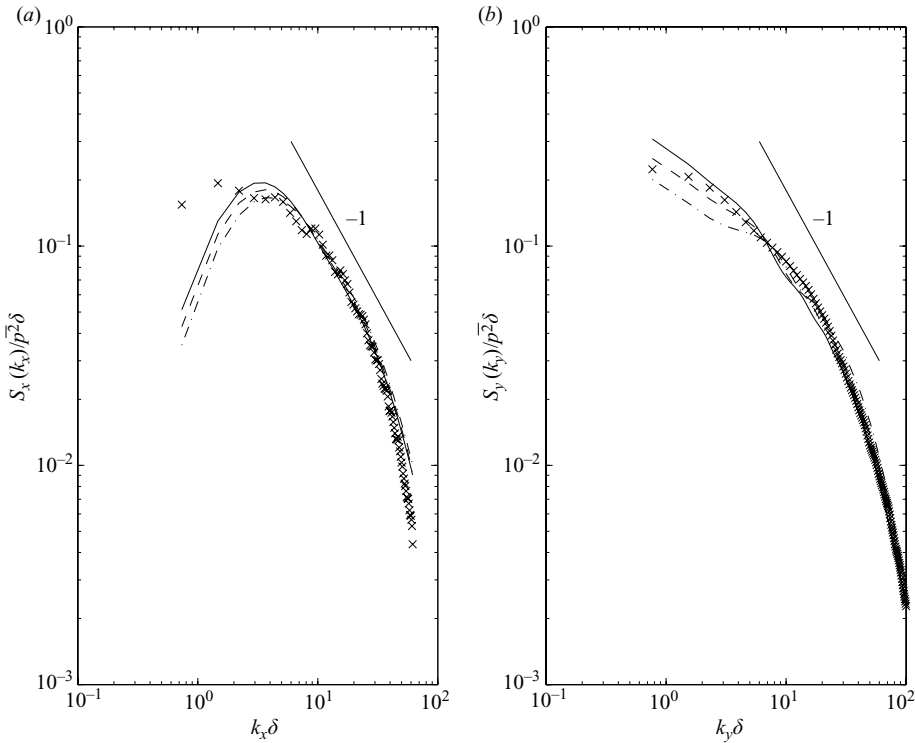


FIGURE 11. One-dimensional wavenumber spectra for the LES test case: (a) streamwise spectrum; (b) spanwise spectrum. Symbol and lines: \times , LES; —, $L = \lambda$; - -, $L = 2^{1/4}\lambda$; - · -, $L = \sqrt{2}\lambda$. Inverse-wavenumber dependence would be parallel to the lines marked ‘-1’.

omitted for the sake of improved clarity in the region where the correlation takes significant values.)

Similar to the spectra, aspect-ratio variations have a weaker effect in the streamwise direction. When L is increased from λ to $\sqrt{2}\lambda$, the zero crossing occurs slightly sooner, as does the recovery from negative values. None of the curves fits the measurements perfectly, but that for largest L is probably the most successful.

A similar observation applies to the spanwise results. Here the measurements are straddled by the $L = 2^{1/4}\lambda$ and $L = \sqrt{2}\lambda$ curves. Of these two, the latter gives the best agreement in absolute terms.

4.2.3. The Tu-144LL flight-test data

Figure 13 shows the (nominally) streamwise and spanwise correlations for the Tupolev 144LL flight test, normalized as previously. Owing to the much greater boundary-layer thickness attained here, the normalized separations are smaller than Blake’s, but for consistency the same scales are used.

In general, the comparison between prediction and measurement yields observations similar to the Blake case: aspect-ratio variations are more significant for spanwise separations, with no single curve passing perfectly through all data points; however, good overall agreement in both directions is found for the highest aspect ratio: $L = \sqrt{2}\lambda$.

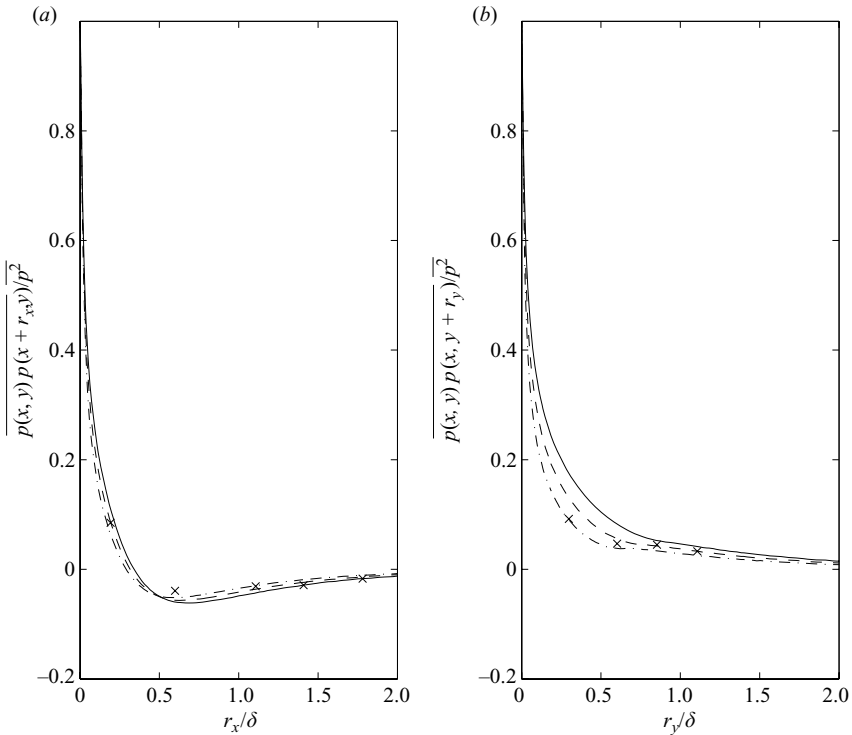


FIGURE 12. One-dimensional correlation functions for the Blake test case: (a) streamwise; (b) spanwise. Symbol and lines: \times , data; —, $L = \lambda$; - -, $L = 2^{1/4}\lambda$; - · -, $L = \sqrt{2}\lambda$.

4.3. Off-axis results

In the light of the on-axis comparisons, it appears that the appropriate value of the base-eddy aspect ratio varies slightly with Reynolds number, from $L/\lambda = 2^{1/4}$ for the LES results to $L/\lambda = \sqrt{2}$ for the laboratory-scale and flight-test data. This may well be ascribable to uncertainty in the data and/or the other model parameters, rather than of physical significance. Nonetheless, here we use that information to set a single aspect ratio for each prediction. As before, the data sets are presented in order of increasing Reynolds number.

4.3.1. Singer's LES data

The predicted two-dimensional spectrum for base eddies with $L = 2^{1/4}\lambda$ is shown in figure 14(a). It is normalized in the same way, and over the same wavenumber range, as its one-dimensional counterparts. The corresponding LES spectrum is plotted alongside in figure 14(b). The absence of complete statistical convergence is clearly evident in its oscillatory nature. Nonetheless, the overall topology is clear and compares quite well with that of the predicted spectrum. (Note, in particular, the greater width of the peak in the spanwise wavenumber direction, and its offset from the origin along the streamwise wavenumber axis.) An obvious discrepancy is in the height of the peak; the predicted levels at and around $k_x = 0$ are also markedly lower than those obtained from the LES data.

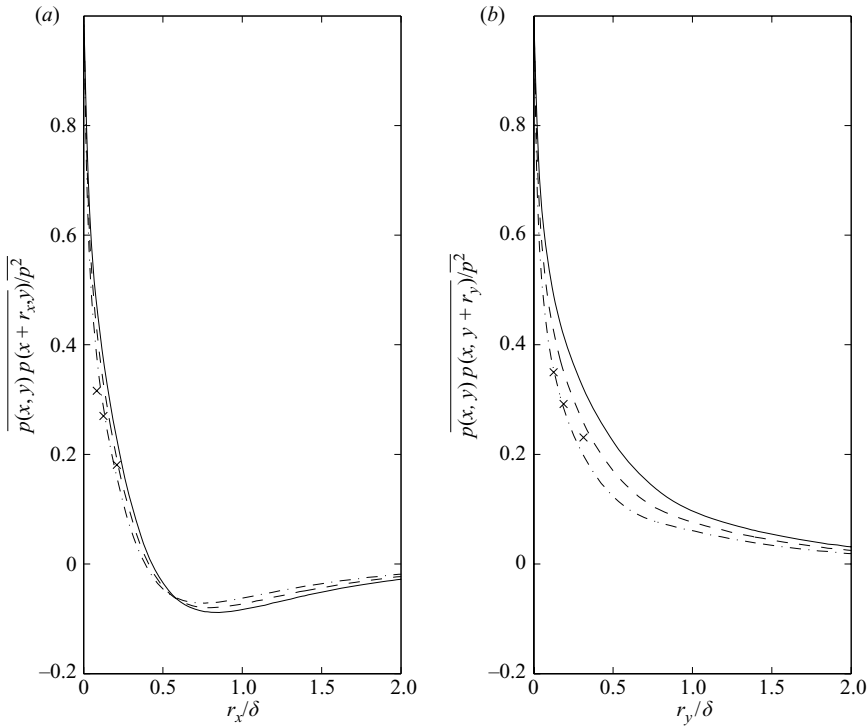


FIGURE 13. One-dimensional correlation functions for the Tu-144LL test case: (a) (near-)streamwise; (b) (near-)spanwise. Symbol and lines: \times , data; $—$, $L = \lambda$; $- -$, $L = 2^{1/4}\lambda$; $- \cdot -$, $L = \sqrt{2}\lambda$.

4.3.2. Bull's wind tunnel data

As noted previously, Blake's wind tunnel data set does not include off-axis correlations and, in their absence, we turn to the results of Bull (1967), taken at a comparable Reynolds number. The contours deduced by Bull from his correlation measurements are reproduced in the left-hand half of figure 15. In the right-hand half are the corresponding predictions for base-eddy geometry $L = \sqrt{2}\lambda$. There is clearly strong qualitative agreement with the experimental data. Equally, though, a quantitative comparison shows a significant difference: the extent of the predicted correlation field is notably smaller than that of Bull's construction.

4.3.3. The Tu-144LL flight-test data

Only four oblique correlations are available from the transducer arrangement of figure 10, and each of these is at a different angle (48.6° , 52.7° , 64.0° and 73.7°). The values are thus shown together in figure 16, along with the predicted correlation curves for the four angles.

All the measured correlation values are very similar, and the range of separations is relatively small, so the experimental data points form a single cluster. The 25° angle range available has a rather weak effect on the predicted correlations, which furthermore converge at around the experimental separation distance. All the measured values lie below the predictions, but the discrepancies are not great.

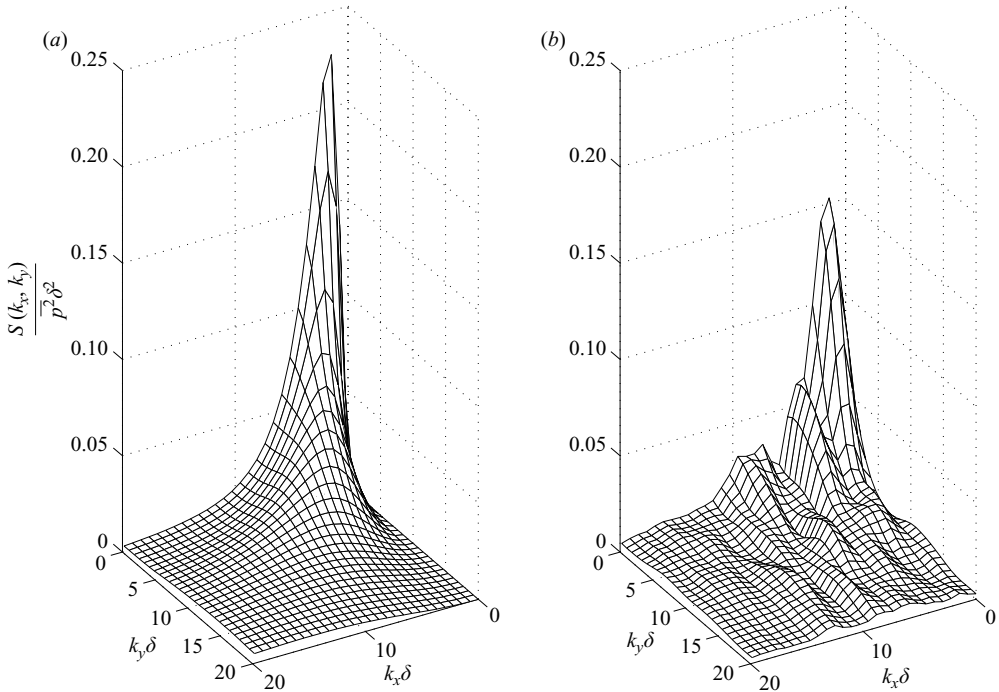


FIGURE 14. Two-dimensional wavenumber spectra for the LES test case: (a) predicted, with $L = 2^{1/4}\lambda$; (b) LES.

4.4. Discussion

Before assessing the implications of our comparisons, it is worth considering what is expected of the theoretical model. Although the fundamental, horseshoe-like, topology of the base eddy is well established, the choice of specific geometry is arbitrary, and here it was based on analytical convenience. The scale integral introduces further adjustable parameters in the form of its limits. Bearing these points in mind, we would not seek to apply the model in a strictly numerical, predictive sense. Instead, its potential value lies in the conceptual insight that it can provide, and its implications for the physical structure of the wall-pressure field. In this context, it can be viewed as successful if it reproduces the fundamental features of the field, for reasonable choices of the base-eddy geometry and the adjustable parameters.

The accuracy of the model's predictions is most easily judged from the one-dimensional, on-axis comparisons. This approach, however, presumes that there are no gross differences in the associated two-dimensional fields that are either missed (for correlations) or integrated out (for spectra). We first, therefore, note that the off-axis comparisons confirm that. This is clearest for the LES spectra, where the entire two-dimensional field is available. However, it is also hard to envisage a realistic two-dimensional correlation structure that admitted the agreement found for the Tu-144LL data at the angles available, but exhibited wild differences in between. This claim is supported by the qualitative topological comparison with the Bull data. (Note, moreover, that the quantitative discrepancy – a narrower predicted structure – is also a feature of Witting's prediction, which is markedly sharper than ours. However, Blake's suggestion that this is due to spatial filtering by Bull's transducers is not supported, since this effect has been accounted for in our choice of lower scale limit.)

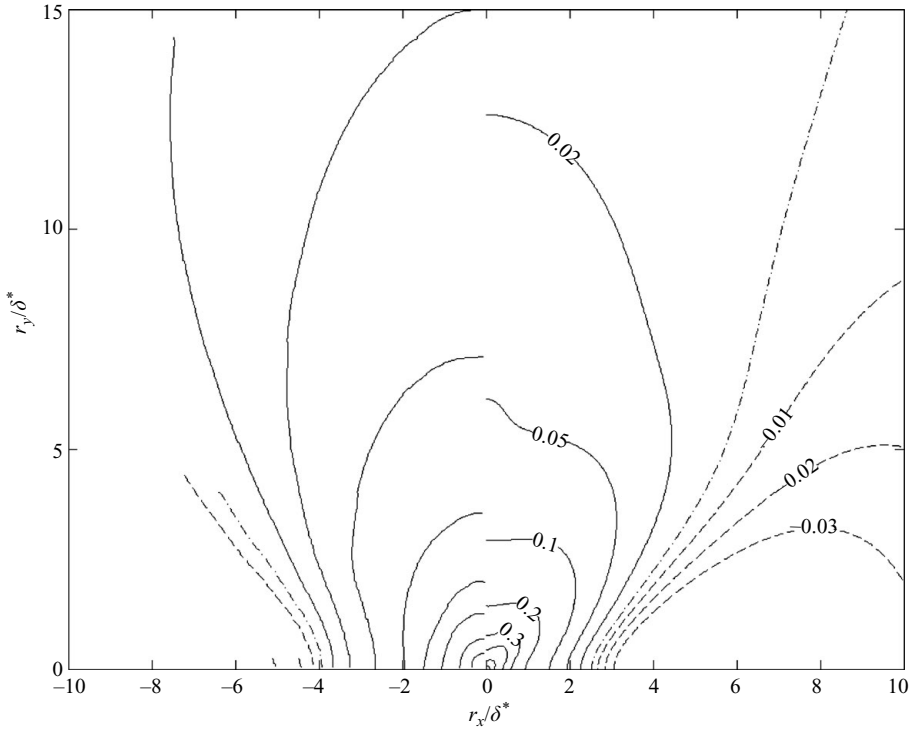


FIGURE 15. Two-dimensional pressure correlations for the Bull test case: (left) experimental; (right) predicted ($L = \sqrt{2}\lambda$). Lines —, positive contour levels (unlabelled at 0.4, 0.6, 0.8); - · -, zero contour level; - -, negative contour levels. Note that Bull used displacement thickness to normalize separations; predicted values are converted to the same scale assuming that $\delta^* = \delta/8$.

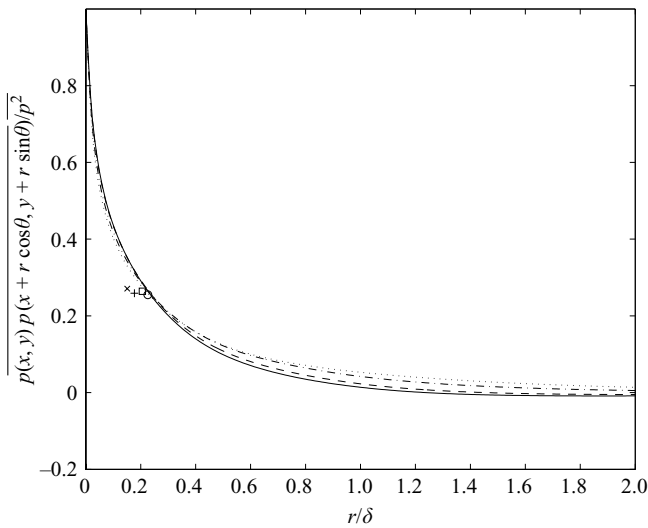


FIGURE 16. Off-axis correlation functions for the Tu-144LL test case. Symbols show data for different angles, θ ; \times , 48.6° ; $+$, 52.7° ; \circ , 64.0° ; \square , 73.7° . Lines give predictions with $L = \sqrt{2}\lambda$; —, 48.6° ; - -, 52.7° ; - · -, 64.0° ; · · ·, 73.7° .

Turning, then, to the streamwise and spanwise comparisons, we first observe that the requirement to reproduce the fundamental features of the data sets, given realistic values of the adjustable parameters, is clearly satisfied by the model. In fact, given the opportunity to choose an optimum base-eddy aspect ratio, even the detail agreement is creditable. Although the introduction of another variable parameter could be regarded as undesirable, it should be noted that the aspect-ratio variation with Reynolds number is very weak, and its qualitative trend matches that observed by Head & Bandyopadhyay (1981).

Limitations in the number of spatial separations obtainable experimentally mean that we are unable to check detail agreement between predicted and measured correlations over their entire range. Nonetheless, the Tu-144LL and Blake data combine to cover separations between 0.1δ and 2δ , beyond which correlation levels are, in any case, very small. Over this range, there are no obvious systematic discrepancies in the comparisons.

In contrast, despite good overall agreement, there is a region in the LES comparisons that merits further attention: the low-wavenumber extreme of the streamwise spectrum. As well as base-eddy aspect ratio, the values here also depend on the upper limit of the scale integral. One could thus argue for a change in this limit to shift the peak in the predicted streamwise spectrum closer to that in the LES data. In our view, however, such a change would be unjustified. There is some physical support for the value chosen, based on empirically observed narrow-band convection velocities. Furthermore, even if one were prepared to neglect this, a change in the limit would have significant effects on the overall breadth of the predicted correlations for the Blake and Tu-144LL data. We regard the consistency of scale-integral upper limit across the different test cases as a strength of the model, and have thus not allowed it to vary.

Two more likely alternative sources for the discrepancy have been identified. The first is the finite streamwise extent of the LES domain. This sets the available wavenumber resolution which, while sufficient to provide a data point below $k_x\delta = 1$, may not be enough to prevent contamination from higher, neighbouring points due to the ‘leakage’ inevitable in spectrum estimation from finite data sets. This hypothesis cannot, unfortunately, be tested by simulating the same phenomenon theoretically, as the spectra from different scale eddies all have different absolute resolution, so the only option is to ensure that it is satisfactory in all cases.

The second lies in the modelling approach, namely the assumption of uncorrelated eddies. If, as seems increasingly to be accepted, the eddies are actually organized in streamwise packets, the corresponding large-scale streamwise correlation will lead to exactly what we observe in figure 14: higher than predicted spectrum levels at low $k_x\delta$.

Finally, we note that the spectral results provide support for the predicted existence of a ‘ k^{-1} ’ range where the level is proportional to the inverse of wavenumber (see, e.g. Blake 1986), at least in the streamwise case. The significance of this observation is probably greatest for the LES data, though. Although the attached-eddy model does not automatically predict a k^{-1} region in the wall-pressure spectra (cf. velocity spectra, where it does, e.g. Nickels *et al.* 2005), it is probable that one will emerge. To see why, consider the simplified one-dimensional case where the eddy spectrum is genuinely universal across the entire scale range, i.e. $P_{ex}(k_x, y, \lambda) = (1/2)\rho u_\tau \Gamma \tilde{P}_{ex}(k_x\lambda, y/\lambda)$, and is of significant magnitude only over a range of dimensionless wavenumbers, $\tilde{k}_a \leq k_x\lambda \leq \tilde{k}_b$. The scale integral for the streamwise spectrum can now be written as

$$S_x(k_x) \sim \left(\frac{1}{2}\rho u_\tau^2\right)^2 \int_{\lambda_{\min}}^{\lambda_{\max}} F(k_x\lambda) d\lambda,$$

where the function $F(\tilde{k})$ arises from the integral of $|\tilde{P}_{ex}(k_x \lambda, y/\lambda)|^2$ over y/λ . Now, if the range of scales is sufficient that $k_x \lambda_{min} < \tilde{k}_a$ and $k_x \lambda_{max} > \tilde{k}_b$, then the limits can be replaced by \tilde{k}_a/k_x and \tilde{k}_b/k_x . Finally, a change of integration variable gives

$$S_x(k_x) \sim \frac{\left(\frac{1}{2}\rho u_\tau^2\right)^2}{k_x} \int_{\tilde{k}_a}^{\tilde{k}_b} F(\tilde{k}) d\tilde{k},$$

which exhibits inverse dependence on the wavenumber k_x . Like the corresponding region in the velocity spectra, this feature will become more evident for greater scale ranges, i.e. increasing Reynolds numbers.

To conclude, then, by the criterion introduced at the beginning of this discussion, we assert that our implementation of an attached-eddy model for wall pressures is successful. It is thus worth considering specific contributions that it might make to the improvement of empirical wall-pressure representations. An unresolved issue here (see, e.g. Singer 1996*b*) is the off-axis form of the wavenumber-frequency spectrum, and this is precisely the kind of information one might extract from the current model. To do so, however, will require the introduction of time dependence, a significant extension which we regard as a fruitful avenue for future work.

5. Conclusions

In this paper, we have applied the attached-eddy model, developed from Townsend's ideas by Perry and co-workers, to the modelling of wall-pressure fluctuations beneath a turbulent boundary layer. As part of this process, we have proposed a novel distribution of eddy geometries for the defect-law region above the logarithmic layer. The results have been compared against numerical and experimental data spanning two decades of Reynolds number. For physically admissible values of the adjustable parameters, the predictions of the model are in good agreement, both qualitative and quantitative, with the test data sets. Furthermore, the model is not highly sensitive to changes in the adjustable parameters. Finally, it gives tentative support for the view that the ratio of eddy length to breadth increases with boundary-layer Reynolds number.

We thus conclude that, as in its application to velocity spectra, the attached-eddy model provides a conceptual framework which enhances our understanding of the wall-pressure field. More specifically, it has the potential to contribute to the advancement of empirical representations of this quantity, by providing a rational basis for the extrapolation of (necessarily limited) experimental data. Further development is, however, required, because it is the wavenumber-frequency spectrum of the wall pressures that is required for vibration prediction. This will require an extension of the attached-eddy model to include time dependence explicitly, and with greater fidelity than via Taylor's hypothesis.

This work was supported by a Korean Government Scholarship and a Lundgren Research Award from the University of Cambridge. The authors would like to thank Dr. Tim Nickels of the Department of Engineering, University of Cambridge, for helpful discussions and advice, and Dr. Bart Singer of NASA Langley for providing his LES data for comparison purposes.

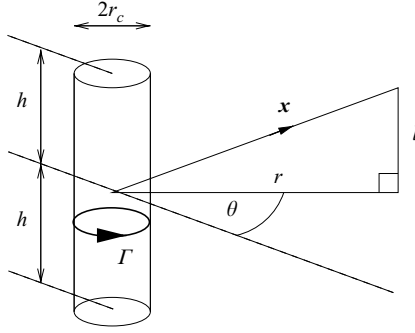


FIGURE 17. Coordinate system and nomenclature for the Biot–Savart analysis of a straight, cylindrical, Rankine vortex element.

Appendix A. The Biot–Savart integral for a cylindrical vortex element

The well-known Biot–Savart expression for the velocity field $\mathbf{u}(\mathbf{x})$ associated with a vorticity field $\boldsymbol{\omega}(\mathbf{x})$ is

$$\mathbf{u}(\mathbf{x}) = \frac{1}{4\pi} \int \frac{\boldsymbol{\omega}(\mathbf{x}') \times (\mathbf{x} - \mathbf{x}')}{|\mathbf{x} - \mathbf{x}'|^3} d^3\mathbf{x}'.$$

We consider the contribution to this integral due to the line element of figure 17. The element has length $2h$, and its vorticity is uniformly distributed in a core of radius r_c . The analysis proceeds most straightforwardly in the polar coordinate system shown in the figure, in terms of which we have $\mathbf{x} = (r, \theta, l)$, $\mathbf{x}' = (r', \theta', l')$ and $\boldsymbol{\omega} = (\Gamma/\pi r_c^2)\mathbf{e}_l$, where Γ is the circulation of the element. The Biot–Savart integral becomes

$$\mathbf{u}(\mathbf{x}) = \frac{\Gamma \mathbf{e}_\theta}{4\pi^2 r_c^2} \int_0^{r_c} \int_0^{2\pi} \int_{-h}^h \frac{r - r' \cos(\theta' - \theta)}{[(l' - l)^2 + D^2]^{3/2}} dl' r' d\theta' dr',$$

where

$$D^2 = r^2 + r'^2 - 2rr' \cos(\theta' - \theta).$$

The integral over l' is straightforward, resulting in

$$\mathbf{u}(\mathbf{x}) = \frac{\Gamma \mathbf{e}_\theta}{4\pi^2 r_c^2} \int_0^{r_c} \int_0^{2\pi} \frac{r - r' \cos(\theta' - \theta)}{D^2} \left[\frac{h - l}{\sqrt{(h - l)^2 + D^2}} + \frac{h + l}{\sqrt{(h + l)^2 + D^2}} \right] r' d\theta' dr', \tag{A 1}$$

but further exact analytical progress is difficult. (The integral over θ' yields an expression involving elliptic integrals of the third kind that does not appear to be integrable over r' .) We therefore consider approximations to (A 1).

Our first assumption is that the element is slender, i.e. $h/r_c \gg 1$. If this condition holds, two useful approximate results can be derived. The first applies far from the core, when $r \gg r_c$ (and hence $r \gg r'$ also). On expanding the terms in D^2 and integrating, one obtains

$$\mathbf{u}(\mathbf{x}) \sim \frac{\Gamma \mathbf{e}_\theta}{4\pi r} \left[\frac{h - l}{\sqrt{(h - l)^2 + r^2}} + \frac{h + l}{\sqrt{(h + l)^2 + r^2}} + O\left(\frac{r_c^2}{r^2}\right) \right]. \tag{A 2}$$

Here the leading-order term is, of course, the Biot–Savart result for a line element. The absence of a term at following order suggests that this expression will be useful in practice, even for moderate values of r/r_c .

The second approximation applies for $r \ll h - l, h + l$, i.e. near the element axis (with the exception of the end regions). Here

$$\frac{h - l}{\sqrt{(h - l)^2 + D^2}} \sim 1 - \frac{1}{2} \frac{D^2}{(h - l)^2} + O\left(\frac{r^4}{h^4}\right),$$

with a similar expansion for its counterpart in (A 1). The integrals arising are standard (see, e.g. Gradshteyn & Rizhik 1994) and yield the result

$$\mathbf{u}(\mathbf{x}) \sim \mathbf{u}_{2D} - \frac{\Gamma r \mathbf{e}_\theta}{8\pi} \left[\frac{1}{(h - l)^2} + \frac{1}{(h + l)^2} + O\left(\frac{r^2}{h^4}\right) \right], \tag{A 3}$$

where \mathbf{u}_{2D} is the two-dimensional Rankine vortex velocity field:

$$\mathbf{u}_{2D} = \frac{\Gamma \mathbf{e}_\theta}{2\pi} \frac{r}{\max(r^2, r_c^2)}.$$

We now seek a composite expansion that includes our two asymptotic limits, and also provides a satisfactory approximation for the velocity at both intermediate distances and the element’s ends. For this purpose, a natural, but heuristic, approach would be to combine the two-dimensional and line element results as follows:

$$\mathbf{u}(\mathbf{x}) \simeq \frac{\mathbf{u}_{2D}}{2} \left[\frac{h - l}{\sqrt{(h - l)^2 + r^2}} + \frac{h + l}{\sqrt{(h + l)^2 + r^2}} \right]. \tag{A 4}$$

This expression clearly includes the large r form in (A 2). Less obviously, it is asymptotically equivalent to the small r form for $r \ll h - l, h + l$ (the original conditions) and $r > r_c$. Inside the core, however, it is not consistent. On the other hand, with the slight modification

$$\mathbf{u}(\mathbf{x}) \simeq \frac{\mathbf{u}_{2D}}{2} \left[\frac{h - l}{\sqrt{(h - l)^2 + \max(r^2, r_c^2)}} + \frac{h + l}{\sqrt{(h + l)^2 + \max(r^2, r_c^2)}} \right], \tag{A 5}$$

one obtains a form that is consistent with (A 3) throughout the range in which it holds.

Figure 18 compares the predictions of the two composite expansions with a numerical evaluation of (A 1), on the symmetry plane of an element with $h/r_c = 1$. Even for such a debatably slender case, (A 5) exhibits excellent accuracy across the entire range. Its asymptotic consistency is evident in the core region, where it differs from (A 4).

The other potentially problematic regions lie around the ends of the element. Figure 19 shows the predicted and calculated velocity fields at $l = 0.95h (= 0.95r_c)$. Here, remarkably, the errors are if anything smaller (and decrease further as the end is approached).

In the light of the sweeping assumptions inherent in the choice of eddy geometry, we do not expect errors at the levels found here to be significant, and hence use

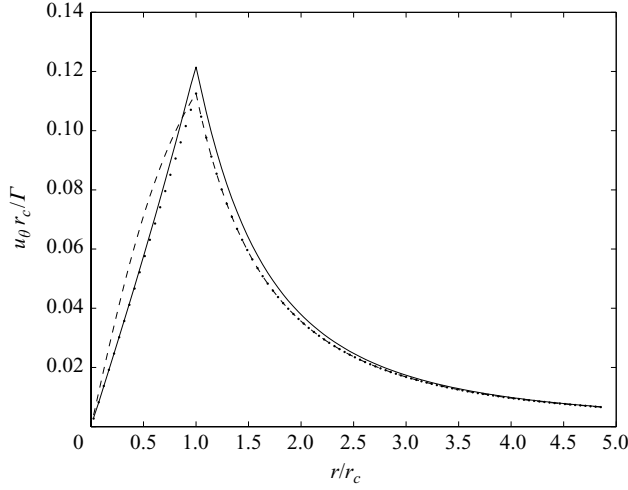


FIGURE 18. Contribution of cylindrical vortex element with $h/r_c=1$ to Biot-Savart integral for tangential velocity at $l=0$. Lines: —, numerical evaluation of (A 1); - -, heuristic approximation, (A 4); · · ·, asymptotic approximation; see (A 5).

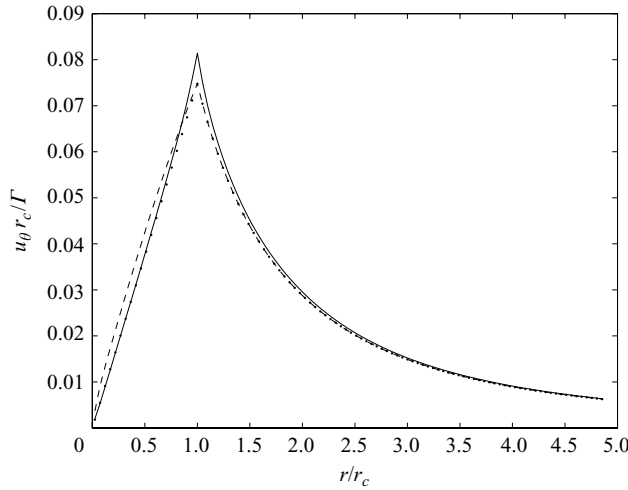


FIGURE 19. Contribution of cylindrical vortex element with $h/r_c=1$ to Biot-Savart integral for tangential velocity at $l=0.95h$. Lines: —, numerical evaluation of (A 1); - -, heuristic approximation, (A 4); · · ·, asymptotic approximation; see (A 5).

(A 5) for velocity calculations throughout the spatial domain. For the z -velocity components of the six straight-line elements that make up our eddy (figure 1), it yields, respectively:

$$w_1(x, y, z) = \frac{\Gamma}{4\pi a^2} \frac{\lambda/2 + y}{\sqrt{2}} \left[\frac{x + z}{\sqrt{(x + z)^2 + 2a^2}} + \frac{\sqrt{2}L - x - z}{\sqrt{(\sqrt{2}L - x - z)^2 + 2a^2}} \right],$$

with

$$a^2 = \max \left(\frac{(x-z)^2}{2} + \left(\frac{\lambda}{2} + y \right)^2, r_c^2 \right);$$

$$w_3(x, y, z) = \frac{\Gamma}{4\pi b^2} \frac{\lambda/2 - y}{\sqrt{2}} \left[\frac{x+z}{\sqrt{(x+z)^2 + 2b^2}} + \frac{\sqrt{2}L - x - z}{\sqrt{(\sqrt{2}L - x - z)^2 + 2b^2}} \right],$$

with

$$b^2 = \max \left(\frac{(x-z)^2}{2} + \left(\frac{\lambda}{2} - y \right)^2, r_c^2 \right);$$

$$w_2(x, y, z) = \frac{\Gamma}{4\pi d^2} \frac{L - \sqrt{2}x}{\sqrt{2}} \left[\frac{\lambda/2 + y}{\sqrt{(\lambda/2 + y)^2 + d^2}} + \frac{\lambda/2 - y}{\sqrt{(\lambda/2 - y)^2 + d^2}} \right],$$

with

$$d^2 = \max \left(\frac{(x-z)^2}{2} + \frac{(\sqrt{2}L - x - z)^2}{2}, r_c^2 \right);$$

$$w_4 = -\frac{\Gamma}{4\pi e^2} \frac{\lambda/2 - y}{\sqrt{2}} \left[\frac{x-z}{\sqrt{(x-z)^2 + 2e^2}} + \frac{\sqrt{2}L - x + z}{\sqrt{(\sqrt{2}L - x + z)^2 + 2e^2}} \right],$$

with

$$e^2 = \max \left(\frac{(x+z)^2}{2} + \left(\frac{\lambda}{2} - y \right)^2, r_c^2 \right);$$

$$w_6 = -\frac{\Gamma}{4\pi f^2} \frac{\lambda/2 + y}{\sqrt{2}} \left[\frac{x-z}{\sqrt{(x-z)^2 + 2f^2}} + \frac{\sqrt{2}L - x + z}{\sqrt{(\sqrt{2}L - x + z)^2 + 2f^2}} \right],$$

with

$$f^2 = \max \left(\frac{(x+z)^2}{2} + \left(\frac{\lambda}{2} + y \right)^2, r_c^2 \right);$$

$$w_5 = -\frac{\Gamma}{4\pi g^2} \frac{L - \sqrt{2}x}{\sqrt{2}} \left[\frac{\lambda/2 + y}{\sqrt{(\lambda/2 + y)^2 + g^2}} + \frac{\lambda/2 - y}{\sqrt{(\lambda/2 - y)^2 + g^2}} \right],$$

with

$$g^2 = \max \left(\frac{(x+z)^2}{2} + \frac{(\sqrt{2}L - x + z)^2}{2}, r_c^2 \right).$$

Appendix B. Derivation of the inner velocity profile

Having chosen to specify $U = u_\tau z^+$ for a finite distance from the wall, we wish to avoid the discontinuity in gradient that would arise in subsequently jumping to

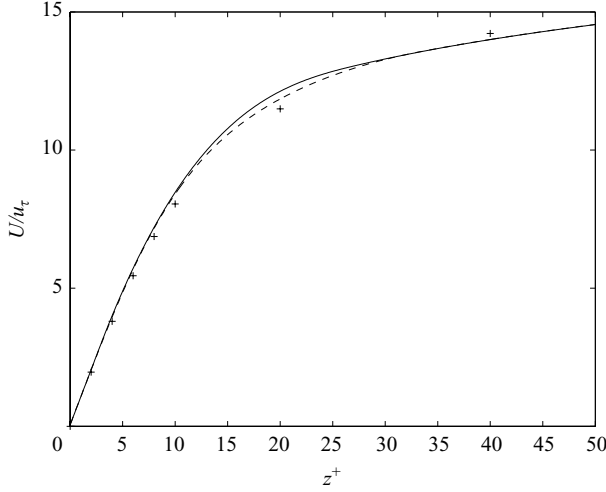


FIGURE 20. The wall region velocity profile. Symbol and lines: +, Coles' experimental data; —, current, from numerical integration of (2.9); - -, Bull, from numerical integration of (2.8.)

Bull's expression; see (2.8). We also note that the latter has a near-linear region for z^+ between 3 and 8. This is well fitted by the line

$$\frac{1}{u_\tau} \frac{dU}{dz^+} = 1 - \frac{z^+ - 2.8}{15.7}.$$

We therefore seek an overall fit extending to the start of the logarithmic region of the form

$$\frac{1}{u_\tau} \frac{dU}{dz^+} = 1 - \frac{z^+ - 2.8}{15.7} + k(z^+ - 2.8)^n,$$

valid up to an (as yet) unspecified switch-over point, $z^+ = z_1^+$. Note that the upper limit on the constant gradient region must now be $z^+ = 2.8$, for continuity.

The values of k , n and z_1^+ are found by requiring continuity of value, gradient and second derivative with the logarithmic velocity profile; see (2.7). These conditions are

$$z_1^+ - \frac{(z_1^+ - 2.8)^2}{31.4} + \frac{k}{n + 1} (z_1^+ - 2.8)^{n+1} = \frac{1}{0.41} \log z_1^+ + 5.0, \tag{B 1}$$

$$1 - \frac{z_1^+ - 2.8}{15.7} + k (z_1^+ - 2.8)^n = \frac{1}{0.41 z_1^+}, \tag{B 2}$$

$$-\frac{1}{15.7} + nk (z_1^+ - 2.8)^{n-1} = -\frac{1}{0.41 (z_1^+)^2}. \tag{B 3}$$

Of these, (B3) can be used to substitute for the terms involving k in the first two, of which (B2) then becomes a straightforward expression for n in terms of z_1^+ . The solution procedure consists of specifying a set of trial values for z_1^+ , finding the associated n s from the development of (B2), and then solving the development of (B1) graphically for z_1^+ . Finally, back-substitution into (B2) and (B3) yields the result quoted in §2.4, namely $k = 4.683 \times 10^{-4}$, $n = 2.262$, $z_1^+ = 27.45$.

Bull's original expression was designed to fit the (discrete) inner region profile data given by Coles (see Schumann & Corcos 1967). In figure 20, we replot these data, along with the integrated forms of (2.8) and (2.9). Although Bull's expression lies

closer to the Coles data point at $z^+ = 20$, there is little to choose between the two; given the assumptions involved in specifying our typical eddy, we expect the effect of the difference to be negligible in this work.

Appendix C. Boundary-layer parameters for the Tu-144LL flight test

The parameters to be estimated are the kinematic viscosity, the boundary-layer thickness and the skin-friction coefficient. The first of these can be deduced with good accuracy from the flight measurements of equivalent airspeed (which implicitly specifies the density) and temperature. The latter is 258.5 K, which yields a dynamic viscosity $\mu = 1.63 \times 10^{-5} \text{ kg m}^{-1} \text{ s}^{-1}$ via Sutherland's law (Schlichting 1979). The equivalent airspeed of 144 m s^{-1} corresponds to a density $\rho = 0.765 \text{ kg m}^{-3}$, giving $\nu = 2.13 \times 10^{-5} \text{ m}^2 \text{ s}^{-1}$.

This leaves the skin-friction coefficient and boundary-layer thickness to be determined. For the latter, Rizzi *et al.* (2000) quote two empirical corrections to the well-known 1/7th-power law for the incompressible boundary layer at a distance x along a flat plate (see, e.g. Young 1989), the Boeing formula

$$\delta = 0.37xRe_x^{-1/5} \left[1 + \left(\frac{Re_x}{6.9 \times 10^7} \right)^2 \right]^{0.1}, \quad (\text{C1})$$

and the Tupolev formula

$$\delta = 0.37xRe_x^{-1/5} [1 + 0.144M^2]^{0.35}. \quad (\text{C2})$$

In these expressions, Re_x is the Reynolds number based on x and the free-stream velocity. For our fuselage location and flight conditions, they yield values of 0.486 m and 0.344 m, respectively, a considerable difference. Furthermore, no formulae are available for the skin-friction coefficient.

However, once one accepts the approximation of the fuselage boundary layer by its flat-plate equivalent, there is a considerable body of work to draw on. Young (1989) reports that compressibility has little effect on thickness and (at this Mach number) decreases the skin-friction coefficient to 96.7 % of its incompressible value. He also recommends, for the Reynolds numbers of interest to us here, the 1/9th-power-law expressions for the incompressible, flat-plate boundary layer,

$$c_f = 0.0375Re_x^{-1/6},$$

$$\delta = 0.27xRe_x^{-1/6},$$

in preference to their 1/7th-power-law counterparts. On this basis, we obtain $c_f = 1.33 \times 10^{-3}$ and $\delta = 0.479 \text{ m}$, the latter lying between the Boeing and Tupolev estimates. These are the values used in providing the boundary-layer parameters cited for this case in table 1.

REFERENCES

- ADRIAN, R. J. 2007 Hairpin vortex organization in wall turbulence. *Phys. Fluids* **19**, 041301–1–041301-16.
- ADRIAN, R. J., MEINHART, C. D. & TOMKINS, C. D. 2000 Vortex organization in the outer region of the turbulent boundary layer. *J. Fluid Mech.* **422**, 1–54.
- BLAKE, W. K. 1970 Turbulent boundary-layer wall-pressure fluctuations on smooth and rough walls. *J. Fluid Mech.* **44**, 637–660.

- BLAKE, W. K. 1986 *Mechanics of Flow-Induced Sound and Vibration, Vol. 2: Complex Flow-Structure Interactions*. Academic.
- BULL, M. K. 1967 Wall-pressure fluctuations associated with subsonic turbulent boundary layer flow. *J. Fluid Mech.* **28**, 719–754.
- BULL, M. K. 1969 Mean shear in a constant-pressure turbulent boundary layer. *AIAA J.* **7**, 359–362.
- DHANAK, M. R. & DOWLING, A. P. 1995 On the pressure fluctuations induced by coherent vortex motion near a surface. *26th AIAA Fluid Dyn. Conf.* paper 95-2240.
- GRADSHTEYN, I. S. & RIZHIK, I. M. 1994 *Table of Integrals, Series, and Products*. Academic.
- GRAHAM, W. R. 1997 A comparison of models for the wavenumber-frequency spectrum of turbulent boundary layer pressures. *J. Sound Vib.* **206**, 541–565.
- HAMBLETON, W. T., HUTCHINS, N. & MARUSIC, I. 2006 Simultaneous orthogonal-plane particle image velocimetry measurements in a turbulent boundary layer. *J. Fluid Mech.* **560**, 53–64.
- HEAD, M. R. & BANDYOPADHYAY, P. 1981 New aspects of turbulent boundary-layer structure. *J. Fluid Mech.* **107**, 297–338.
- HOWE, M. S. 1989 The rôle of surface shear stress fluctuations in the generation of boundary layer noise. *J. Sound Vib.* **65**, 159–164.
- HUTCHINS, N., HAMBLETON, W. T. & MARUSIC, I. 2005 Inclined cross-stream stereo particle image velocimetry measurements in turbulent boundary layers. *J. Fluid Mech.* **541**, 21–54.
- HUTCHINS, N. & MARUSIC, I. 2007 Evidence of very long meandering features in the logarithmic region of turbulent boundary layers. *J. Fluid Mech.* **579**, 1–28.
- MARUSIC, I. 2001 On the role of large-scale structures in wall turbulence. *Phys. Fluids* **13**, 735–743.
- MARUSIC, I. & PERRY, A. E. 1995 A wall-wake model for the turbulence structure of boundary layers. Part 2. Further experimental support. *J. Fluid Mech.* **298**, 389–407.
- NICKELS, T. B., MARUSIC, I., HAFEZ, S. & CHONG, M. S. 2005 Evidence of the k^{-1} law in a high-Reynolds-number turbulent boundary layer. *Phys. Rev. Lett.* **95**, 074501-1–074501-4.
- NICKELS, T. B., MARUSIC, I., HAFEZ, S., HUTCHINS, N. & CHONG, M. S. 2007 Some predictions of the attached eddy model for a high Reynolds number boundary layer. *Phil. Trans. R. Soc. A* **365**, 807–822.
- PERRY, A. E. & CHONG, M. S. 1982 On the mechanism of wall turbulence. *J. Fluid Mech.* **119**, 173–217.
- PERRY, A. E., HENBEST, S. & CHONG, M. S. 1986 A theoretical and experimental study of wall turbulence. *J. Fluid Mech.* **165**, 163–199.
- PERRY, A. E. & MARUSIC, I. 1995 A wall-wake model for the turbulence structure of boundary layers. Part 1. Extension of the attached eddy hypothesis. *J. Fluid Mech.* **298**, 361–388.
- RIZZI, S. A., RACKL, R. G. & ANDRIANOV, E. V. 2000 Flight test measurements from the Tu-144LL structure/cabin noise experiment. *NASA TM* 2000-209858.
- SCHLICHTING, H. 1979 *Boundary-Layer Theory*. McGraw-Hill.
- SCHUMANN, G. & CORCOS, G. M. 1967 The dynamics of turbulence near a wall according to a linear model. *J. Fluid Mech.* **29**, 113–135.
- SINGER, B. A. 1996a Large-eddy simulation of turbulent wall-pressure fluctuations. *NASA CR* 198276.
- SINGER, B. A. 1996b Turbulent wall-pressure fluctuations: new model for off-axis cross-spectral density. *NASA CR* 198297.
- SPALART, P. R. 1988 Direct simulation of a turbulent boundary layer up to $Re_\theta = 1410$. *J. Fluid Mech.* **187**, 61–98.
- TOWNSEND, A. A. 1976 *The Structure of Turbulent Shear Flow*. Cambridge University Press.
- WITTING, J. M. 1986 A spectral model of pressure fluctuations at a rigid wall bounding an incompressible fluid, based on turbulent structures in the boundary layer. *Noise Control Engng J.* **26**, 28–43.
- WU, X. & MOIN, P. 2009 Direct numerical simulation of turbulence in a nominally zero-pressure-gradient flat-plate boundary layer. *J. Fluid Mech.* **630**, 5–41.
- YOUNG, A. D. 1989 *Boundary Layers*. AIAA Education Series.